AGU PUBLICATIONS

JGR

Journal of Geophysical Research: Oceans

RESEARCH ARTICLE

10.1002/2016JC012334

**Key Points:**
- Nonhydrostatic model NHWAVE is shown to resolve shear instabilities in a stratified shear flow
- Resolved shear instabilities are similar to field observation at comparable Reynolds number
- Surface signatures associated with the front and the shear instabilities are revealed

**Correspondence to:**
Z. Zhou,
zzhou@udel.edu

**Citation:**
Zhou, Z., X. Yu, T.-J. Hsu, F. Shi, W. R. Geyer, and J. T. Kirby (2017), On nonhydrostatic coastal model simulations of shear instabilities in a stratified shear flow at high Reynolds number, *J. Geophys. Res. Oceans*, *122*, 3081–3105, doi:10.1002/2016JC012334.

Received 16 SEP 2016
Accepted 14 MAR 2017
Accepted article online 17 MAR 2017
Published online 11 APR 2017

© 2017. American Geophysical Union. All Rights Reserved.

# On nonhydrostatic coastal model simulations of shear instabilities in a stratified shear flow at high Reynolds number

**Zheyu Zhou[1,2], Xiao Yu[1,3], Tian-Jian Hsu[1], Fengyan Shi[1], W. Rockwell Geyer[4], and James T. Kirby[1]**

[1]Center for Applied Coastal Research, Civil and Environmental Engineering, University of Delaware, Newark, Delaware, USA, [2]AECOM, New York, New York, USA, [3]Institute of Marine Sciences, University of North Carolina at Chapel Hill, Chapel Hill, North Carolina, USA, [4]Applied Ocean Physics and Engineering, Woods Hole Oceanographic Institution, Woods Hole, Massachusetts, USA

**Abstract** The nonhydrostatic surface and terrain-following coastal model NHWAVE is utilized to simulate a continually forced stratified shear flow in a straight channel, which is a generic problem to test the existing nonhydrostatic coastal models' capability in resolving shear instabilities in the field scale. The resolved shear instabilities in the shear layer has a Reynolds number of about $1.4 \times 10^6$, which is comparable to field observed value. Using the standard Smagorinsky closure with a grid size close to the Ozmidov length scale, simulation results show that the resolved energy cascade exceeds 1 order of magnitude and the evolution and turbulent mixing characteristics are predicted well. Two different approaches are used to estimate the turbulent dissipation rate, namely using the resolved turbulent energy spectrum and the parameterized subgrid turbulent dissipation rate, and the predicted results provide the upper and lower bounds that encompass the measured values. Model results show significantly higher turbulence in braids of shear instabilities, which is similar to field observations while both the subgrid turbulent dissipation rate and resolved vorticity field can be used as surrogates for measured high acoustic backscatter signals. Simulation results also reveal that the surface velocity divergence/convergence is an effective identifier for the front of the density current and the shear instabilities. To guide future numerical studies in more realistic domains, an evaluation on the effects of different grid resolutions and subgrid viscosity on the resolved flow field and subgrid dissipation rate are discussed.

## 1. Introduction

In estuaries or river mouths where riverine water meets seawater, flow structures can be highly complex due to density stratification, flow instabilities, and their interactions with bathymetry. The frontal zone, defined here as the sharp transition between freshwater and seawater, is highly dynamic both spatially and temporally [e.g., *Garvine and Monk*, 1974; *Garvine*, 1975; *O'Donnell et al*., 2008; *Giddings et al*., 2012]. Various flow structures are generated which manifest the sharp transition of flow properties (e.g., salinity) at different scales, such as internal waves and shear instabilities [e.g., *Chickadel et al*., 2009; *Nash et al*., 2009; *Geyer et al*., 2010]. These flow structures can enhance mixing of freshwater and nutrients. Moreover, large mixing can further result in high turbidity due to suspended particulate matter that can scatter light and affect water clarity. Some of these flow structures are sufficiently intense to impact navigation safety and can leave unique surface signatures which can be detected by remote sensing imagery [*Plant et al*., 2009, 2010a, 2010b; *Chickadel et al*., 2011].

Among all these flow structures, the most generic one is the shear instabilities generated at a stably stratified shear flow. Shear instabilities are responsible for the major turbulent dissipation and vertical mixing in a river plume [e.g., *MacDonald and Geyer*, 2004; *Orton and Jay*, 2005; *Geyer et al*., 2010], particularly in the frontal zone. In many river plume models [e.g., *Garvine*, 1974; *O'Donnell*, 1990], the parameterizations of vertical mixing/dissipation at the base of the plume control the accuracy of the model prediction. A commonly used parameterization assumes the magnitude of vertical mixing/dissipation decays exponentially with distance from the front [*Garvine*, 1974]. However, it was only until more recently that this assumption can be validated with direct field measurement, for instance, the Connecticut River plume observation reported by *O'Donnell et al*. [2008]. With an aim to resolve energy-containing turbulence, this study begins to tackle the

challenge of resolving shear instabilities in a field-scale stratified shear flow using a surface and terrain-following ($\sigma$-coordinate) nonhydrostatic coastal model. Lessons learned from this numerical investigation may provide insights for more complicated river plume simulations in the future.

Regional-scale coastal/ocean models assuming hydrostatic pressure are often used to study ocean-estuary exchange processes on intratidal or spring-neap tidal timescales. To cover large estuarine and shelf regions of several tens to hundreds of kilometers, relatively coarse resolution of O(100) meter mesh size in two horizontal directions is applied. The coarse resolution is consistent with the assumption that processes resolved by O(100) meter meshes are often hydrostatic, with a large ratio of horizontal length scale to vertical length scale. This modeling approach is not designed to resolve shear instabilities at the density interface. However, when appropriate effective viscosity in the horizontal directions and turbulence closure in the vertical direction are incorporated [e.g., *Ralston et al*., 2010; *Scully et al*., 2011; *Elias et al*., 2012], these models can capture the overall mixing and bulk frontal dynamics through Reynolds-averaged eddy-viscosity type modeling strategy.

On the other hand, when the main objective is to study and predict dynamics in a frontal zone (sharp density interfaces), fine horizontal resolution is needed and the resolved processes may become increasingly nonhydrostatic. For instance, the nonhydrostatic coastal ocean model SUNTANS [*Fringer et al*., 2006] with unstructured-grid was demonstrated to accurately predict the formation of a front in the Snohomish River estuary in comparison with remote sensing imagery [*Plant et al*., 2009; *Wang et al*., 2009, 2011]. Recently, SUNTANS was also used to study the mixing and sediment resuspension associated with the propagation of internal bores in a shallow bay [*Masunaga et al*., 2015]. The model successfully reproduced the fine features associated with the runup of the internal bore and the vortex motion at the bore head. The nonhydrostatic version of FVCOM was also used to simulate tidally generated internal wave in Massachusetts Bay [*Lai et al*., 2010]. These studies demonstrated the capability of nonhydrostatic models in resolving frontal dynamics and dispersion of internal waves when high spatial resolution is used.

A number of recent field studies have revealed the importance of small-scale features in coastal environments that motivate the application of nonhydrostatic and turbulence-resolving models for field-scale flows. Using thermal infrared imaging, *Chickadel et al*. [2009] observed surface disruption by vertical propagating boils as an intense tidal flow propagates over a rocky sill in Snohomish River estuary. These boils are essentially turbulent coherent structures and of particular significance was that the resulting surface signatures detected by thermal infrared imagery may allow further estimation of flow field and turbulent dissipation rate [*Chickadel et al*., 2011]. *Geyer et al*. [2010] collected field data at two along-river transects in the Connecticut River estuary to understand shear instabilities and turbulent mixing in a river plume. They observed that, in a continually forced river plume at high Reynolds number of about $\mathrm{Re} = 0.5 \times 10^6$ (defined based on half shear layer thickness and half velocity difference across the shear layer) secondary instabilities within the braids (the thin filaments connecting the cores) of the shear instabilities are the dominant mechanism causing turbulent dissipation and mixing. Their field observation is distinct from many laboratory [e.g., *Simpson*, 1972, 1982; *Koop and Browand*, 1979; *Caulfield et al*., 1996] and direct numerical simulation (DNS) [see for example, *Smyth and Moum*, 2000; *Smyth et al*., 2001] studies of decaying shear layer (or lock exchange) at lower Reynolds number where turbulent mixing occurs primarily in the cores of shear instability as a result of the gravitational collapse of the statically unstable fluid rolled up within the cores [*Geyer et al*., 2010]. This finding is significant because observation of mixing in the braids as a result of secondary instability in the oceanic mixing was rare. In the literatures, secondary instabilities were first theorized by *Corcos and Sherman* [1976], and later demonstrated by 2-D numerical simulations [*Staquet*, 1995] and laboratory observations [*Atsavapranee and Gharib*, 1997]. Although surface disruptions associated with these shear instabilities are not measured in field observations of *Geyer et al*. [2010], it can be expected that these shear instabilities, particularly the braids, may leave notable surface signatures.

To advance the modeling of mixing, shear instabilities, and surface signatures in field-scale stratified flows, it may be essential to resolve the general structure of cores and braids while assuming that the secondary instabilities can be parameterized with a subgrid closure, since their contribution is mainly to energy dissipation. As we will discuss in this paper, the aforementioned proposition is not straightforward. Using the nonhydrostatic coastal ocean model NHWAVE [*Ma et al*., 2013; *Shi et al*., 2017], a direct implementation of k-$\varepsilon$ closure with submeter mesh size gives large turbulent diffusion and the braid structure of shear instabilities cannot be resolved (see Figure 2, more detail to be discussed later). Using the nonhydrostatic coastal

ocean model MITgcm [*Marshall et al*., 1997], *Stashchuk and Vlasenko* [2009] and *Vlasenko et al*. [2013] simulated the generation and evolution of internal waves of the Columbia River plume observed by *Nash and Moum* [2005]. *Stashchuk and Vlasenko* [2009] adopted a prescribed vertical viscosity that further depends on local Richardson number. For stably stratified conditions in the Columbia River plume, the resulting vertical mixing coefficient (or eddy viscosity) is around $O(10^{-3})$ $m^2/s$ and they are able to better resolve internal wave dynamics at the plume front. Therefore, in the context of coastal ocean modeling, the parameterization of turbulent viscosity/diffusivity plays a key role in determining the flow structures that can (or cannot) be resolved while in the meantime, one needs to ensure that such parameterization leads to accurate prediction of the overall kinetic energy dissipation and mixing characteristics.

Accurate parametrizations of subgrid turbulent viscosity/diffusivity is not trivial. Recently, *Mashayek and Peltier* [2011, 2012a, 2012b, 2013] carried out a series of direct numerical simulation of shear instabilities at high Reynolds number (up to 10,000). They show that the secondary instability is the primary mechanism driving transition to turbulence at high Reynolds number although there are a range of mechanisms that are responsible for the secondary instabilities. At a high Reynolds number of $Re = 5 \times 10^4$, *Pham and Sarkar* [2014] adopted the large-eddy simulation approach to resolve shear instabilities in a shear layer. With a mesh size about three times smaller than the Ozmidov length scale, they demonstrated that the evolution and turbulent mixing characteristics are predicted very well in the simulation.

Through significantly improved remote sensing technology, researchers have become interested in understanding coherent structures in estuaries and their particular surface signatures [e.g., *Chickadel et al*., 2009; *Horner-Devine et al*., 2013; *Honegger*, 2015]. For this purpose, it is highly desirable that typical nonhydrostatic surface-following and terrain-following ($\sigma$-coordinate) coastal ocean models can be used to simulate coherent structures. However, to model coherent structures using nonhydrostatic coastal ocean models remains rare [*Shi et al*., 2017]. One of the modeling challenges is due to the large amount of computational resource needed to cover the head, body, and lift-off region of the density current and meanwhile to resolve (or partially resolve) the shear instabilities. To simulate the head of a gravity current while avoiding a long domain, *Scotti* [2008] adopted a Galilean coordinate transformation methodology in a direct numerical simulation so that the head is fixed within the computational domain. However, this approach is not applicable for more general flow conditions. The purpose of this study is to begin to address this challenge using a nonhydrostatic $\sigma$-coordinate coastal ocean model. We apply one of such models NHWAVE [*Ma et al*., 2013; *Shi et al*., 2017] to simulate field-scale shear instabilities at a Reynolds number comparable to that observed in *Geyer et al*. [2010]. As a first step, we focus on simulation in an idealized domain of a long rectangular channel that covers the lift-off, the body and the head of the propagating density current. The remaining of the paper is organized as follow. In section 2, the governing equations and numerical schemes are discussed, followed by a discussion on model setup in section 3. Model results are present in section 4 and further discussions are given in section 5. Concluding remarks are given in section 6.

## 2. Model Formulation

### 2.1. Governing Equation

The numerical model NHWAVE is utilized in this study to simulate shear instabilities in a buoyant plume. NHWAVE was originally developed to model three-dimensional (3-D), fully dispersive, fully nonlinear surface wave propagation in free-surface and terrain-following coordinates [*Ma et al*., 2012]. Exploiting the nonhydrostatic and $\sigma$-coordinate capabilities in the numerical model, *Ma et al*. [2013] extended NHWAVE for a nonhydrostatic ocean/coastal model by adding the capabilities of solving salinity and suspended sediment transport and the corresponding baroclinic flow. The extended NHWAVE was verified/validated with a lock-exchange density current problem reported in other numerical studies [*Härtel et al*., 2000; *Fringer et al*., 2006; *Lai et al*., 2010] and measured data obtained in a laboratory turbidity/density current experiment [*Garcia*, 1993]. More recently, NHWAVE was used to simulate the formation of an internal hydraulic jump and the generation of finger patterns near the North Jetty in the mouth of Columbia River during ebb flow [*Shi et al*., 2017]. When high spatial resolution and fine time step are used, we adopt NHWAVE in this study to resolve stratified shear layer and shear instabilities using the large-eddy simulation (LES) strategy.

The filtered mass and momentum equations describing the resolved flow motion and the corresponding subgrid turbulence closure are first presented. The mass conservation equation for incompressible flow in transformed $\sigma$-coordinates is given as [*Ma et al*., 2013]

$$\frac{\partial D}{\partial t}+\frac{\partial Du}{\partial x}+\frac{\partial Dv}{\partial y}+\frac{\partial \omega}{\partial \sigma}=0 \tag{1}$$

where $D=h+\eta$ is total local depth, $h$ is still water depth, and $\eta$ is the surface elevation. In this study, $u$, $v$, $w$ represent velocity components in the Cartesian coordinate system ($x^*$, $y^*$, $z^*$), and $\omega$ is the vertical velocity defined in the transformed $\sigma$-coordinate system ($x$, $y$, $\sigma$) given as

$$\omega=\left(\frac{\partial h}{\partial t}-\sigma\frac{\partial D}{\partial t}\right)+u\left(\frac{\partial h}{\partial x}-\sigma\frac{\partial D}{\partial x}\right)+v\left(\frac{\partial h}{\partial y}-\sigma\frac{\partial D}{\partial y}\right)+w \tag{2}$$

The generalized governing equations for momentum conservation can be written as

$$\frac{\partial D\boldsymbol{U}}{\partial t}+\nabla\cdot\Theta(\boldsymbol{U})=\boldsymbol{S} \tag{3}$$

where the vector $\Theta(\boldsymbol{U})$ represents the momentum fluxes given as

$$\Theta(\boldsymbol{U})=\begin{pmatrix}\left(Duu+\left(\frac{1}{2}g\eta^2+gh\eta\right)\right)\boldsymbol{i}+Duv\boldsymbol{j}+u\omega\boldsymbol{k}\\ Duv\boldsymbol{i}+\left(Dvv+\left(\frac{1}{2}g\eta^2+gh\eta\right)\right)\boldsymbol{j}+v\omega\boldsymbol{k}\\ Duw\boldsymbol{i}+Dvw\boldsymbol{j}+w\omega\boldsymbol{k}\end{pmatrix} \tag{4}$$

The source term $\boldsymbol{S}$ on the right hand side includes the following components:

$$\boldsymbol{S}=\boldsymbol{S}_h+\boldsymbol{S}_p+\boldsymbol{S}_\rho+\boldsymbol{S}_\tau \tag{5}$$

where $\boldsymbol{S}_h$, $\boldsymbol{S}_p$, $\boldsymbol{S}_\rho$, and $\boldsymbol{S}_\tau$ represent the bottom slope effect, the dynamic pressure gradient, the baroclinic forcing, and the stress term, respectively, and they are given by

$$S_h=\begin{pmatrix}gD\frac{\partial h}{\partial x}\\ gD\frac{\partial h}{\partial y}\\ 0\end{pmatrix},\quad S_p=\begin{pmatrix}-\frac{D}{\rho}\left(\frac{\partial p}{\partial x}+\frac{\partial p}{\partial \sigma}\frac{\partial \sigma}{\partial x^*}\right)\\ -\frac{D}{\rho}\left(\frac{\partial p}{\partial y}+\frac{\partial p}{\partial \sigma}\frac{\partial \sigma}{\partial y^*}\right)\\ -\frac{1}{\rho}\frac{\partial p}{\partial \sigma}\end{pmatrix},\quad S_\rho=\begin{pmatrix}-gD\left(\frac{\partial r}{\partial x}+\frac{\partial r}{\partial \sigma}\frac{\partial \sigma}{\partial x^*}\right)\\ -gD\left(\frac{\partial r}{\partial y}+\frac{\partial r}{\partial \sigma}\frac{\partial \sigma}{\partial y^*}\right)\\ -g\frac{\partial r}{\partial \sigma}\end{pmatrix} \tag{6}$$

where $p$ is the dynamic pressure and $r$ is the baroclinic pressure head calculated by

$$r=\frac{D}{\rho_0}\int_\sigma^1\rho d\sigma \tag{7}$$

with $\rho$ the fluid density and $\rho_0$ the reference density. The stress terms are given as

$$S_\tau=\begin{pmatrix}DS_{\tau x}\\ DS_{\tau y}\\ DS_{\tau z}\end{pmatrix} \tag{8}$$

where $S_{\tau x}$, $S_{\tau y}$, and $S_{\tau z}$ represent the total stress including both viscous stresses and subgrid turbulent stresses. In this study, we use the standard Smagorinsky model as turbulence closure, where the turbulent stress is given as $S_{\tau,\ ij}=2D\left(\nu_{sgs}+\nu\right)\frac{\partial u_i}{\partial x_j}$ with the molecular viscosity represented by $\nu$ and the subgrid turbulent viscosity is written as

$$\nu_{sgs}=C_s^2\left(\Delta_x\Delta_y\Delta_z\right)^{2/3}\sqrt{S_{ij}S_{ij}} \tag{9}$$

where $\Delta_x$ and $\Delta_y$ are grid sizes in the two horizontal directions. In the vertical direction, the grid size $\Delta_z$ is calculated based on the water depth $h$ and surface elevation $\eta$ following $\Delta_z=\Delta_\sigma(h+\eta)$, with $\Delta_\sigma$ kept as a constant. Standard value of Smagorinsky constant $C_s=0.2$ is used in this study [*Meneveau and Katz*, 2000].

The surface elevation can be obtained from the continuity equation (1), which is rewritten as

$$\frac{\partial D}{\partial t}+\frac{\partial}{\partial x}\left(D\int_0^1 ud\sigma\right)+\frac{\partial}{\partial y}\left(D\int_0^1 vd\sigma\right)=0 \tag{10}$$

As the fluid density $\rho$ depends on salinity $s$ with a constitutive equation [*Ma et al.*, 2013], the conservation equation for salinity $s$ is given as

$$\frac{\partial Ds}{\partial t}+\nabla\cdot\boldsymbol{\theta}(\boldsymbol{s})=\boldsymbol{S}_s \tag{11}$$

The vector form of the convection term is given by

$$\boldsymbol{\theta}(\boldsymbol{s})=(Dus,\ \ Dvs,\omega s) \tag{12}$$

On the right-hand side of equation (11), $S_s$ represents the total diffusion term, which include the subgrid molecular diffusion and the turbulent diffusion, namely, $S_s=D\nabla\cdot(\kappa\nabla s)$ with $\kappa$ representing the total diffusivity of the salinity. Here the total diffusivity $\kappa$ is set to be the sum of molecular diffusivity and subgrid turbulent diffusivity and the Prandtl number is assumed to be constant and equal to unity.

### 2.2. Numerical Scheme

NHwave uses a combined finite-volume and finite difference scheme with a Godunov-type method for the spatial discretization and a two-stage (second-order) SSP Runge-Kutta (R-K) scheme [*Gottlieb et al.*, 2001] for the time integration [*Ma et al.*, 2012, 2013]. The two-step predictor-corrector projection method is applied to solve the dynamic pressure. Here we only illustrate the first stage of R-K scheme. In the predictor step, velocity at the intermediate step $\mathrm{U}^*$, is evaluated by

$$\frac{\mathrm{U}^*-\mathrm{U}^n}{\Delta t}=-\nabla\cdot\Theta(\mathrm{U})^n+\mathrm{S}_h^n+\mathrm{S}_\rho^n+\mathrm{S}_\tau^n \tag{13}$$

where $\mathrm{U}^n$ is the velocity vector at previous time step n. In the corrector step, the intermediate velocity field is corrected to satisfy the continuity equation:

$$\frac{\mathrm{U}^{(1)}-\mathrm{U}^*}{\Delta t}=\mathrm{S}_p^{(1)} \tag{14}$$

where the superscript $()^{(1)}$ represents the first stage of R-K scheme. The dynamic pressure term $\mathrm{S}_p^{(1)}$ is solved by the pressure Poisson equation

$$\frac{\partial}{\partial x}\left[\frac{\partial p}{\partial x}+\frac{\partial p}{\partial\sigma}\frac{\partial\sigma}{\partial x^*}\right]+\frac{\partial}{\partial y}\left[\frac{\partial p}{\partial y}+\frac{\partial p}{\partial\sigma}\frac{\partial\sigma}{\partial y^*}\right]+\frac{\partial}{\partial\sigma}\left(\frac{\partial p}{\partial x}\right)\frac{\partial\sigma}{\partial x^*}+\frac{\partial}{\partial\sigma}\left(\frac{\partial p}{\partial y}\right)\frac{\partial\sigma}{\partial y^*}+\left[\left(\frac{\partial\sigma}{\partial x^*}\right)^2+\left(\frac{\partial\sigma}{\partial y^*}\right)^2+\frac{1}{D^2}\right]\frac{\partial}{\partial\sigma}\left(\frac{\partial p}{\partial\sigma}\right)$$
$$=\frac{\rho}{\Delta t}\left(\frac{\partial u^*}{\partial x}+\frac{\partial u^*}{\partial\sigma}\frac{\partial\sigma}{\partial x^*}+\frac{\partial v^*}{\partial y}+\frac{\partial v^*}{\partial\sigma}\frac{\partial\sigma}{\partial y^*}+\frac{1}{D}\frac{\partial w^*}{\partial\sigma}\right) \tag{15}$$

The incomplete Cholesky GMRES is used to solve the linear system shown above. The same procedure is carried out for the second stage of R-K scheme. The velocity at the final stage is calculate as

$$\mathrm{U}^{(n+1)}=\frac{\mathrm{U}^{(1)}+\mathrm{U}^{(2)}}{2} \tag{16}$$

The transport of salinity is then calculated using the updated velocity field after the corrector step. For the grid arrangement, velocity components and tracer variables are stored/defined at the cell centers. The dynamic pressure is defined at the cell face following the Keller-box scheme. The velocity values at the cell faces, $(u^*, v^*, w^*)$, are reconstructed by linear interpolation using the adjacent cell-centered values for the discretization of the Poisson equation. The time step is determined by the CFL criterion with the Courant number set to be 0.5. A hybrid linear parabolic approximation scheme (HLPA) [*Zhu*, 1991] is applied for the spatial discretization of equation (11).

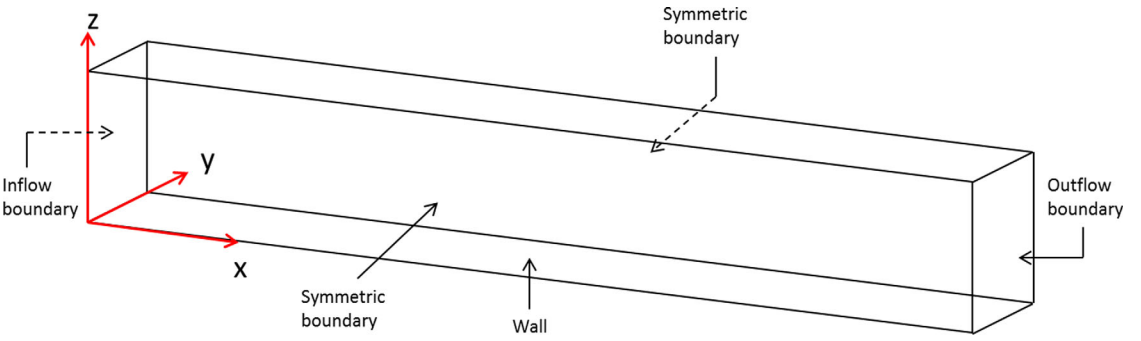


**Figure 1.** A sketch of the computational domain.

## 3. Model Setup

3-D numerical simulations are carried out to model shear instabilities in a stratified shear layer of a density current and the resulting surface signatures in an idealized domain. The simulation domain is a straight channel with a flat bottom. The size of the domain and flow parameters are chosen such that the resulting shear layer characteristics and shear instabilities are similar to the field observations reported by *Geyer et al.* [2010] where the Reynolds number of the measured shear instability is approximately $Re = 5\times10^5$. Hence, the domain length is determined to be 500 m in the streamwise (x) direction and the initial water depth is set to be 10 m (see Figure 1). Several different domain widths (y-direction) are tested to ensure that it is sufficiently large to encompass the largest eddies (see Table 1). Initially the fluid is at rest with salinity of 26 psu. Fresh water (zero salinity) is sent from the left inflow boundary, with a prescribed log-law velocity profile with a depth-averaged velocity of 0.6 m/s. To stabilize the simulation, the inflow is introduced to the system gradually within the first 60 s of the simulation. An open outflow boundary is implemented at the right boundary, and a wall boundary is applied at the bottom. Symmetric (free slip) boundary condition is used for the two lateral boundaries, in which the velocity normal to the boundaries, and the gradients of salinity and velocity parallel to the wall are set to be zero. Due to the simplicity of the model domain, the main focus of this study is on modeling shear instabilities at the density interface and their resulting surface signatures in the density current. Perturbations to the initial velocity or salinity field are not prescribed to ensure that no instability mode is favored over the others. When the density current develops, shear instabilities are generated and the most unstable mode or the dominant wave number can be identified from the simulation results.

To better resolve shear instabilities, a uniform grid is used in the two horizontal directions. To provide the main motivation of this study, a 3-D simulation is first carried out for coarse resolution (total number of grid point $N_{tot} = 12.8 \times 10^6$) with the k-$\varepsilon$ closure (Case 0, the documentation for the Reynolds-averaged Navier-Stokes model and the k-$\varepsilon$ closure in NHWAVE can be found in *Ma et al.* [2013] and *Derakhti et al.* [2016]). Results from Case 0 with the k-$\varepsilon$ closure are then contrasted with another 3-D simulation using the same grid resolution but with the standard Smagorinsky closure (Case 1). As we will demonstrate in section 4.1, Case 0 is able to predict the bulk characteristics of the density current and the shear layer via a large turbulent viscosity/diffusivity calculated by the k-$\varepsilon$ closure. However, it is not able to resolve shear instabilities in the present idealized domain. On the other hand, the simulation with the standard Smagorinsky closure (Case 1) can resolve the large-scale motion of shear instabilities and their surface signatures with reasonable shear layer characteristics, although the grid size is several times larger than the estimated Ozmidov length scale. As our goal is to predict shear instabilities in a stratified shear layer, section 4.2 is devoted to Case 2,

**Table 1.** A Summary of Simulations Presented in This Study

| Case No. | $N_{tot} \times 10^6$ | $L_x \times L_y \times L_z$ (m) | $N_x \times N_y \times N_z$ | $\Delta x$ (m) | $\Delta y$ (m) | $\Delta\sigma$ | Closure |
|---|---|---|---|---|---|---|---|
| Case 0 | 12.8 | 500 × 38.4 × 10 | 1000 × 128 × 100 | 0.5 | 0.3 | 0.01 | k-$\varepsilon$ |
| Case 1 | 12.8 | 500 × 38.4 × 10 | 1000 × 128 × 100 | 0.5 | 0.3 | 0.01 | Standard Smagorinsky |
| Case 2 | 80 | 500 × 40.96 × 10 | 3125 × 256 × 100 | 0.16 | 0.16 | 0.01 | Standard Smagorinsky |
| Case 3 | 40 | 500 × 40 × 10 | 2000 × 200 × 100 | 0.25 | 0.2 | 0.01 | Standard Smagorinsky |

in which a high resolution 3-D simulation ($N_{tot} = 80 \times 10^6$) with the standard Smagorinsky closure is carried out to evaluate the resolved shear instabilities, turbulent mixing and shear layer characteristics. An intermediate resolution simulation (Case 3 with $N_{tot} = 40 \times 10^6$) is also carried out to evaluate the effect of grid resolution on the resolved flow features.

## 4. Model Results

### 4.1. Reynolds-Averaged Modeling Approach Versus Eddy-Resolving Simulation Approach

The Reynolds-averaged modeling approach has been widely used in the study of stratified flow. For example, *Ilicak et al*. [2008] tested the performance of different Reynolds-averaged closure with the regional ocean modeling system (ROMS) for the simulations of the Red Sea overflow. *Wang et al*. [2009] adopted SUNTANS with the Mellor-Yamada level 2.5 closure to simulate the interaction of the tides with complex bathymetry in the macrotidal Snohomish River estuary. The same model and turbulence closure were used by *Masunaga et al*. [2015] to study the internal bores at Otsuchi Bay in Japan. Comparisons of the results of Case 0 (Reynolds-averaged model with the k-$\varepsilon$ closure) and Case 1 (eddy-resolving via the standard Smagorinsky closure) are first discussed to contrast the difference of these two approaches and to motivate the high resolution simulations to be investigated in section 4.2. In these two runs, same grid resolution of $\Delta x = 0.5$ m, $\Delta y = 0.3$ m, and $\Delta z \approx 0.1$ m (100 vertical sigma layer in an initial flow depth of 10 m) is used. Figure 2a shows a snapshot of Case 0 for the salinity field at the center plane ($y = 15$ m) at $t = 350$ s. The development of a density current can be clearly seen. The density current lifts off immediately entering the domain, and with a rapid increase of flow velocity in the near field, a couple of shear instability billows are formed (see $x = 10$–$40$ m). However, these billows quickly disappear, which are then followed by the development of a rather well-mixed stably stratified shear layer between $x = 100$ and 350 m. The model also predicts the frontal region of the density current located between $x = 360$ and 420 m. In other words, Case 0 predicts the development of buoyant density current with the expected front, body and lift-off regions.

Mixing in the stratified flow can be quantified by the Richardson number. The bulk Richardson number is defined as

$$Ri_b = \frac{g\Delta\rho\delta_\omega}{\rho\Delta U^2} \tag{17}$$

where $\delta_\omega$ is the thickness of the mix/shear layer and $\Delta\rho$ and $\Delta U$ are the density and velocity difference across the shear layer. In this study, the upper and lower boundaries of the shear layer are determined by salinity, i.e., the lower boundary is defined where the salinity is 26 psu, while the upper boundary is set at the elevation where salinity drops to 0. The bulk Richardson number represents the ratio of potential energy due to stable stratification to turbulent kinetic energy due to shear and the validity of a model can be evaluated based on the predicted value of $Ri_b$. Figure 2b shows the evolution of bulk Richardson number in the streamwise direction at $t = 350$ s. In between $x = 10$ m and $x = 70$ m, the generation of shear instabilities drives significant mixing and $Ri_b$ is around 0.2. As the billows amalgamate further downstream due to large turbulent diffusion provided by the k-$\varepsilon$ model, the main body of the plume ($x = 150$–$300$ m) becomes well mixed and $Ri_b$ maintains the expected equilibrium value of 0.25. Further downstream toward the head of the density current, flow again becomes more energetic and $Ri_b$ reduces to as low as 0.1 before it peaks again to 0.4 at the head. At the present numerical resolution, Reynolds-averaged k-$\varepsilon$ closure predicts the evolution of $Ri_b$ following the expected turbulent mixing characteristics. We note that the predicted equilibrium value of $Ri_b$ near 0.25 should be expected due to tuning of the closure coefficient in the buoyancy dissipation term in the $\varepsilon$-equation [e.g., *Umlauf and Burchard*, 2005]. The evolution pattern of $Ri_b$ is also consistent with the large-eddy simulation results reported by *Pham and Sarkar* [2014], in which the temporal evolution of $Ri_b$ is shown to encompass the growth and saturation periods. As discussed previously, *Pham and Sarkar* [2014] simulate the temporal evolution of shear instabilities in a periodic domain and used a no-flux condition at the top boundary. Although their model setup is different from the present simulation, the temporal development of shear instabilities in *Pham and Sarkar* [2014] can be qualitatively compared with the spatial development computed by the present study.

The mixing characteristics in the shear layer can also be evaluated by using the resolved vertical profiles of velocity and salinity. Figures 2c and 2d show the vertical distribution of mean flow velocity and salinity at $x = 250$ m. The mean flow velocity and salinity are calculated as

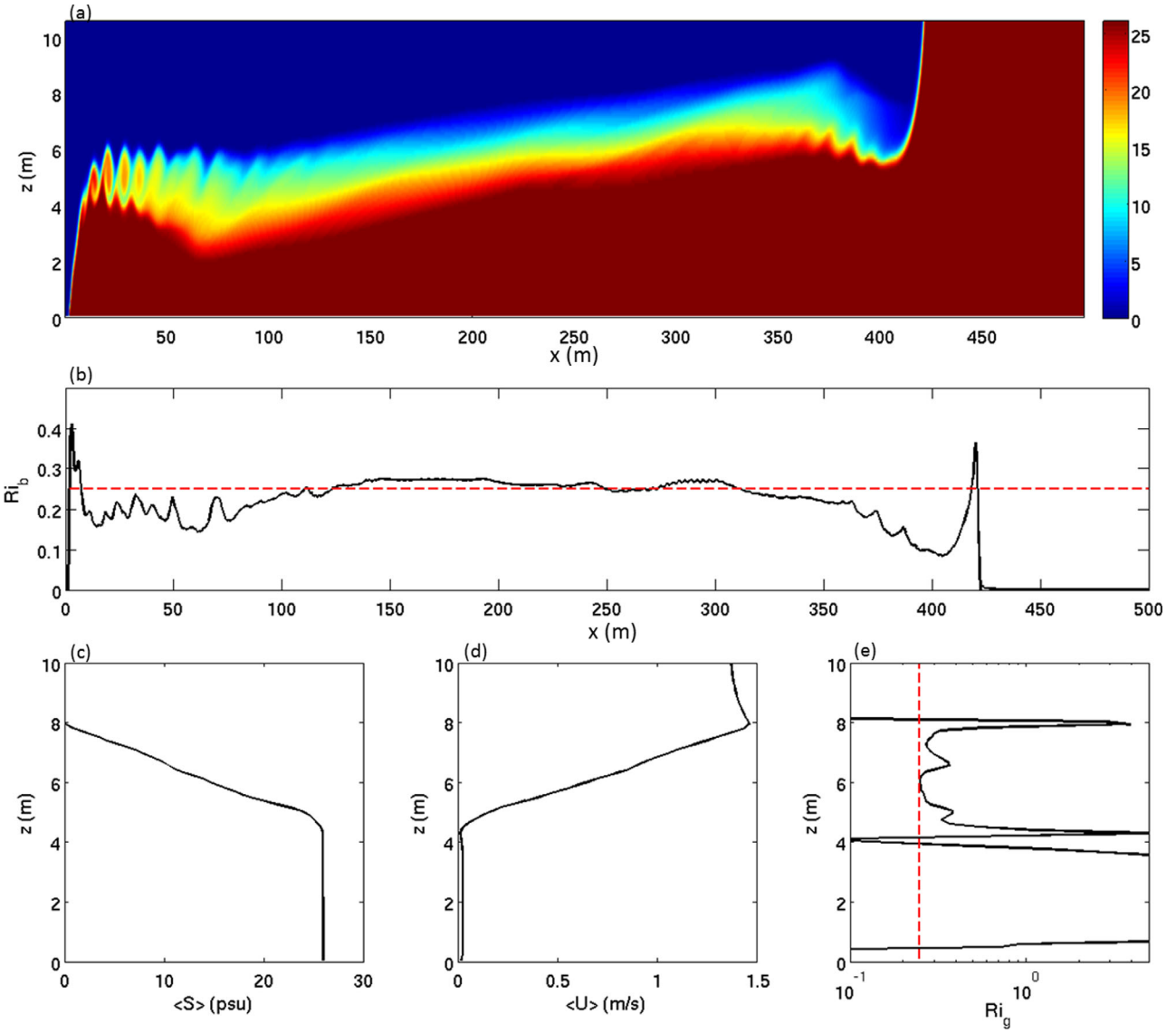


**Figure 2.** (a) Snapshot of salinity distribution at y = 15 m (central plane) at t = 350 s for Case 0 with the k-$\varepsilon$ closure. (b) Streamwise distribution of bulk Richardson number $Ri_b$ and averaged (c) salinity $\langle S \rangle$ (psu), (d) streamwise velocity $\langle U \rangle$ (m/s), and (e) gradient Richardson number $Ri_g$ at x = 250 m. The red dash line in Figures 2b and 2e represent the theoretical critical value 0.25.

$$\langle U \rangle = \frac{1}{L_y}\int_0^{L_y} u dy, \quad \langle S \rangle = \frac{1}{L_y}\int_0^{L_y} s dy \tag{18}$$

where "$< >$" represents spatial averaging over the domain width $L_y$. At this location, the shear layer thickness is close to 3.5 m and the streamwise velocity difference is about 1.4 m/s. The resulting Reynolds number based on half-depth and half of the velocity difference is around $\mathrm{Re} = 1.2 \times 10^6$, which is about two times larger than (but on the same order of magnitude with) that observed in the Connecticut River estuary by *Geyer et al.* [2010]. The salinity and velocity profiles are essentially linear throughout the shear layer. Using the vertical profiles of these averaged flow quantities, the gradient Richardson number is defined as

$$Ri_g = \frac{N^2}{\left(\frac{\partial \langle u \rangle}{\partial z}\right)^2} \tag{19}$$

where $N^2 = -(g/\rho_0)\partial\langle\rho\rangle/\partial z$ is the square of the buoyancy frequency and $\partial\langle u\rangle/\partial z$ is the vertical shear rate. Figure 2e shows the vertical profile of $Ri_g$ at x = 250 m. Outside shear layer, the gradient Richardson number is very

large, suggesting that mixing is very small. However, the $Ri_g$ becomes much lower and in fact approaches (but is slightly greater than) the theoretical critical value 0.25 in the shear layer between z = 5 and 8.0 m. The gradient Richardson number profiles at other locations in the body of the buoyant plume show similar features.

Case 0 with k-$\varepsilon$ closure is able to produce the expected stratified shear layer characteristics. Carefully examining model results of Case 0 indicates that k-$\varepsilon$ closure produces a rather large-eddy viscosity on the order of O($10^{-3}$)–($10^{-2}$) $m^2$/s. However, it is clear that due to such large-eddy viscosity/diffusivity, high wavenumber fluctuations are smoothed out and small-scale features, such as the braid structures of shear instabilities are not resolved even with a submeter scale resolution. Moreover, although model simulation for Case 0 is carried out in completely three-dimensional domain with 128 grid points in the spanwise direction (see Table 1), the resulting flow field is basically two-dimensional with nearly no observable spanwise variability.

With a goal to resolve more structures within shear instabilities in the present study, we pursue an alternative modeling strategy (Case 1) using the standard Smagorinsky closure with the same grid resolution as that used in Case 0. Compared with the eddy-viscosity approach adopted in Case 0, subgrid viscosity calculated by Case 1 is based on the local mesh size and velocity gradient (see equation (9)). Figure 3a shows the

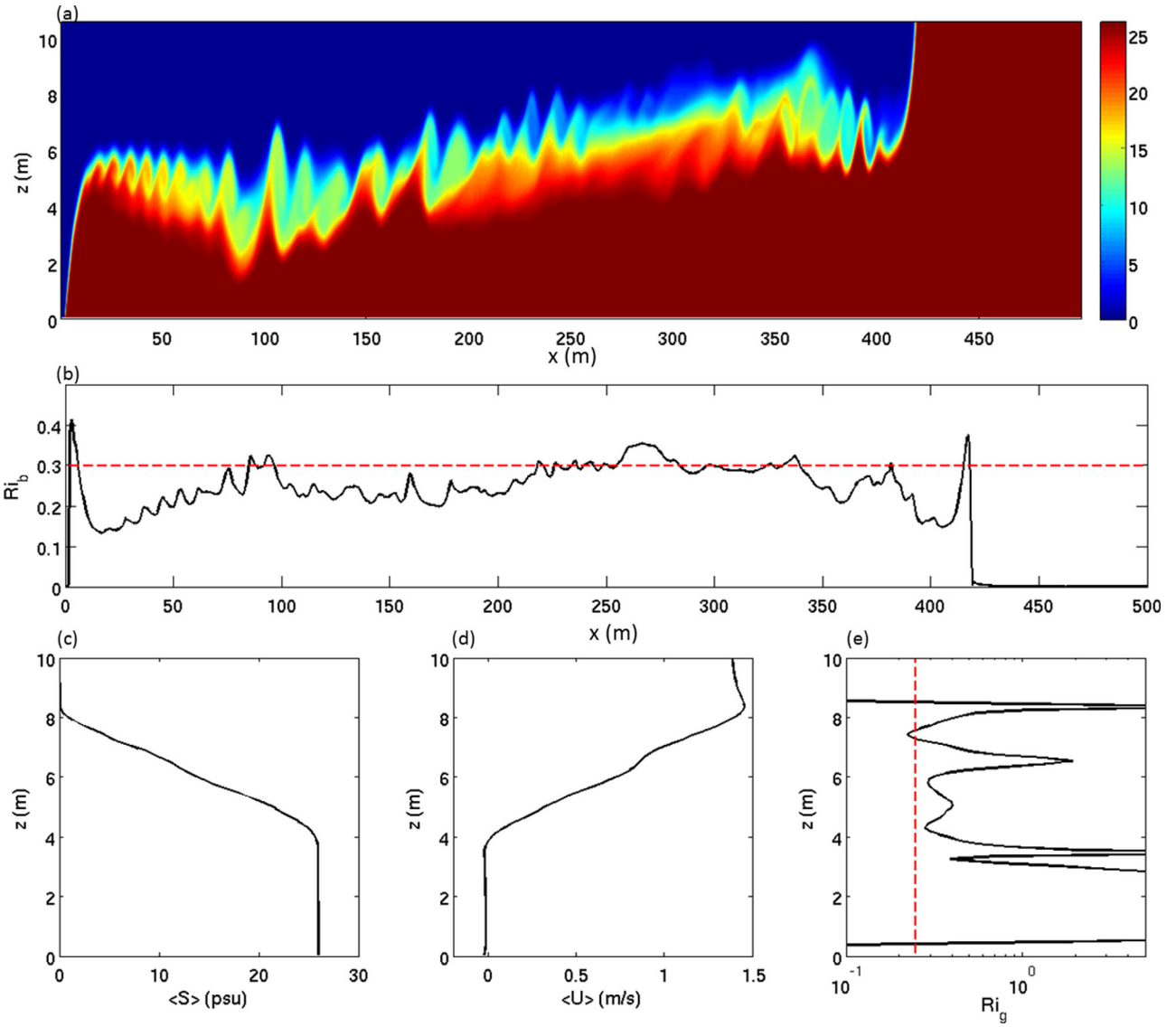


**Figure 3.** (a) Snapshot of salinity distribution at y = 15 m (center plane) at t = 350 s for Case 1 with the standard Smagorinsky closure. (b) Streamwise distribution of bulk Richardson number $Ri_b$ and averaged (c) salinity $\langle S \rangle$ (psu), (d) streamwise velocity $\langle U \rangle$ (m/s), and (e) gradient Richardson number $Ri_g$ at x = 250 m. The red dash line in Figures 3b and e represent the value 0.25.

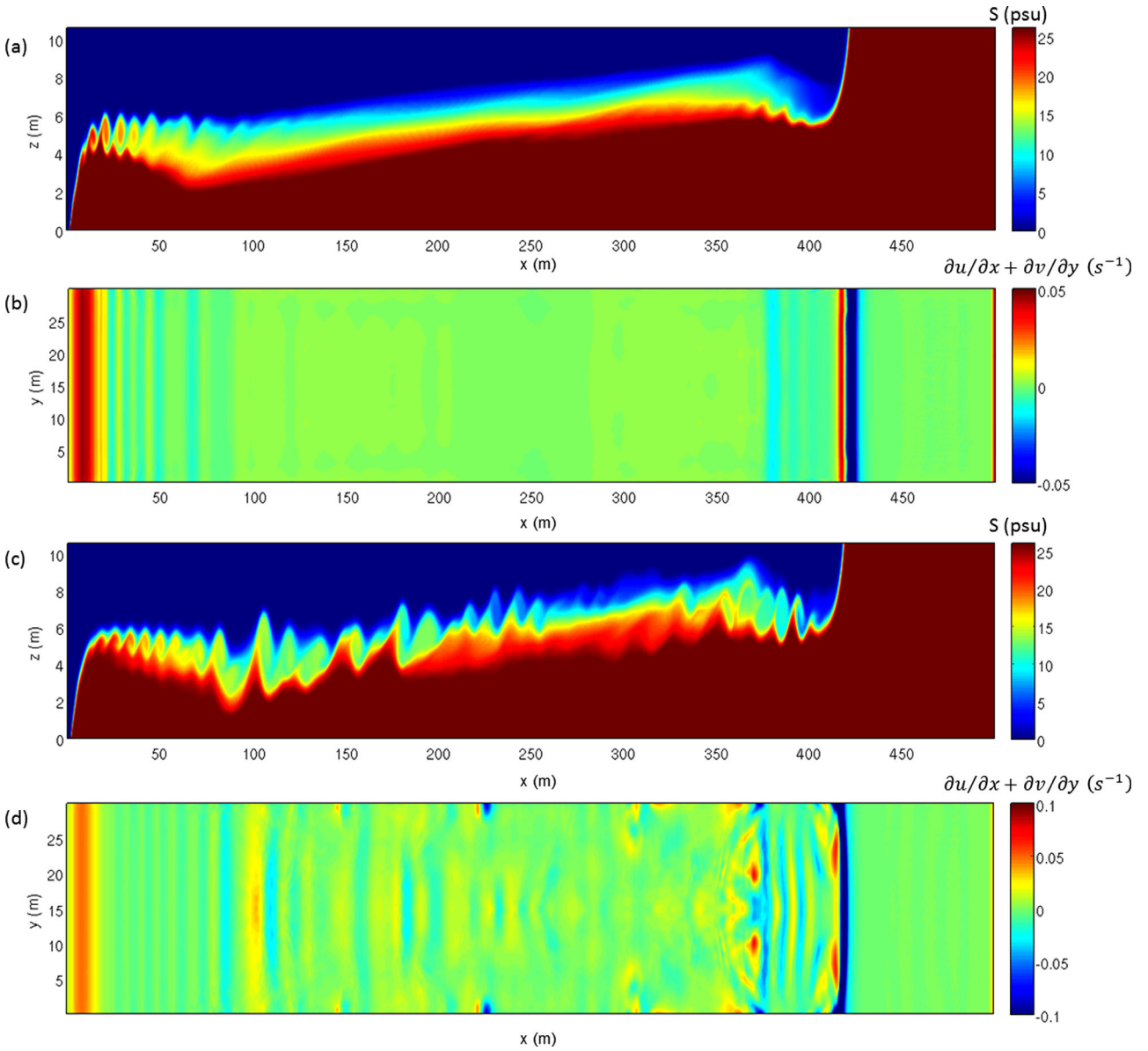


**Figure 4.** (a, b) Snapshots of vertical salinity distribution at y = 15 m (center plane) and surface velocity divergence at t = 350 s for Case 0 (k-$\varepsilon$ closure). (c, d) The corresponding snapshots for Case 1 (standard Smagorinsky model).

snapshot of Case 1 for the salinity field at the center plane (y = 15 m) at t = 350 s. Compared to the salinity field shown in Figure 2a, it is evident that using the standard Smagorinsky closure, more fine-scale structures, particularly the braids of shear instabilities, start to emerge. At this point, the key issue that needs to be addressed is whether the mixing characteristics are appropriately modeled in Case 1. Figure 3b shows the streamwise evolution of bulk Richardson number $Ri_b$ at t = 350 s. The overall evolution of $Ri_b$ is similar to that of Case 0, in particular, $Ri_b$ approaches 0.25–0.3 in the body of the density current when mixing is in equilibrium. From the vertical profiles of averaged velocity and salinity, similar velocity difference is reproduced while the shear layer thickness is about 10% larger. The gradient Richardson number approaches about 0.3 in the shear layer although more fluctuations can be observed.

According to the resolved subgrid viscosity in Case 1, the subgrid viscosity is around $10^{-3}$ $m^2/s$, which is about 1 order of magnitude smaller than the computed eddy viscosity in Case 0. Lower subgrid viscosity allows more fine flow structure to be resolved in Case 1. The resolved fine flow structures give larger local velocity gradients, and interestingly when multiplied by smaller viscosity, the resulting turbulent dissipation

and mixing characteristics appear to be similar to those calculated by k-$\varepsilon$ closure (see more discussion in section 5.3). More detailed investigation on this issue will be given in later sections.

Understanding the distribution of surface signatures and their corresponding water column processes is one of the main reasons to develop the present nonhydrostatic coastal/ocean model [*Shi et al*., 2017] since surface signatures are routinely measured through remote sensing imagery [*Plant et al*., 2009; *Chickadel et al*., 2011]. Following the suggestion by *Plant et al*. [2010b] for radar imagery, positive backscatter signal on the surface may imply strong localized surface strain or horizontal surface convergence. Here the surface signature is set to be represented by the horizontal velocity divergence defined as

$$\nabla_h \cdot \vec{u} = \frac{\partial u}{\partial x} + \frac{\partial v}{\partial y} \tag{20}$$

which is simply the negative of the vertical gradient of the vertical velocity following the continuity equation. Figures 4b and 4d present the horizontal surface velocity divergence for Case 0 and Case 1, respectively. Both figures show strong convergence at the density current front located at x = 420 m. On the other hand, the stationary bottom-hopping density current head located close to the inlet shows notable divergence. Clearly, only Case 1 with the standard Smagorinsky closure may be used to investigate surface signatures associated with shear instabilities. The most notable ones are those immediately upstream of the front (see x = 350–380 m) where a patch of irregular surface signatures associated with shear instabilities near the energetic frontal region can be observed. Throughout the density current, other patches of chaotic surface signatures with weaker intensity can also be seen. In contrast, for Case 0 with k-$\varepsilon$ closure, no such patches can be seen and the resolved flow field is more or less homogeneous in the spanwise (y) direction, i.e., the Reynolds-averaged model reproduces the expected statistically two-dimensional flow.

Although the simulation results using standard Smagorinsky closure can resolve more fine flow structures with acceptable mixing characteristics, more questions arise. In the study of stratified shear flow, most LES studies adopt grid size several times smaller than the Ozmidov length scale [*Pham and Sarkar*, 2014] to ensure that the modeled subgrid-scale turbulence is not deformed by stratification [*Smyth and Moum*, 2000]. According to *Geyer et al*. [2010], the measured turbulent dissipation rate in the shear instabilities ranges between $\varepsilon = 0.8$ and $6.8 \times 10^{-4}$ m$^2$/s$^3$ and the resulting Ozmidov length scale $l_0 = \sqrt{\varepsilon/N^3}$ is about 0.05–0.4 m. Clearly, the grid size used in Case 1 is notably larger than the expected Ozmidov length scale. The reason why numerical results produced by Case 1 show reasonable mixing characteristics is unclear and it is also likely that numerical diffusion plays a role. To answer these questions, high resolution runs are carried out (Case 2 and Case 3) and a more rigorous evaluation are presented in the next section.

### 4.2. High Resolution Simulation Results

We present the highest resolution run (Case 2) in this section and use several methods to demonstrate that the flow field is appropriately resolved. In Case 2, we adopt $\Delta x = \Delta y = 0.16$ m, and $\Delta z \approx 0.1$ m and hence the spatial resolution is similar to the estimated Ozmidov length scale of $l_0 = 0.05$–0.4 m [*Geyer et al*., 2010]. The grid sizes in the streamwise and spanwise directions are chosen to be identical because the resolved turbulence is expected to be more or less isotropic in these two directions. Moreover, the spanwise domain size is also expanded to $L_y = 40.96$ m to ensure that the results are not affected by domain width. Finally, we also carry out Case 3 at an intermediate grid resolution of $\Delta x = 0.25$ m, $\Delta y = 0.2$ m, and $\Delta z \approx 0.1$ m (see Table 1) for evaluating grid convergence.

Figure 5a shows a snapshot of the salinity distribution of the center plane (y = 20 m) at t = 350 s. A density current can be clearly seen with the front located at x = 420 m. Compared to Case 1 of low resolution, the characteristics of the head, the body and the lift-off region are qualitatively similar. To examine the structure of shear instabilities in detail, Figures 5b–5e of further show the coherent structures at different streamwise regions at t = 350 s using the Q-method [*Jeong and Hussain*, 1995]. Close to the inflow boundary (x = 10–40 m), the composite Froude number is 1.35 and the rollers are essentially two dimensional. Flow in this initial stage is not yet turbulent and mixing is weak. Because the 2-D rollers are unstable to three-dimensional disturbances at high Reynolds number, they start to develop into 3-D structures with rib vortices in the braids between the rollers in the region from x = 40 to 100 m (see Figure 5c). Due to more intense turbulence generation, the composite Froude number drops rapidly to 0.8 at around x = 40 m, and the averaged value between x = 40 and 100 m is around 0.85. Further downstream (x = 100–350 m), shear instabilities

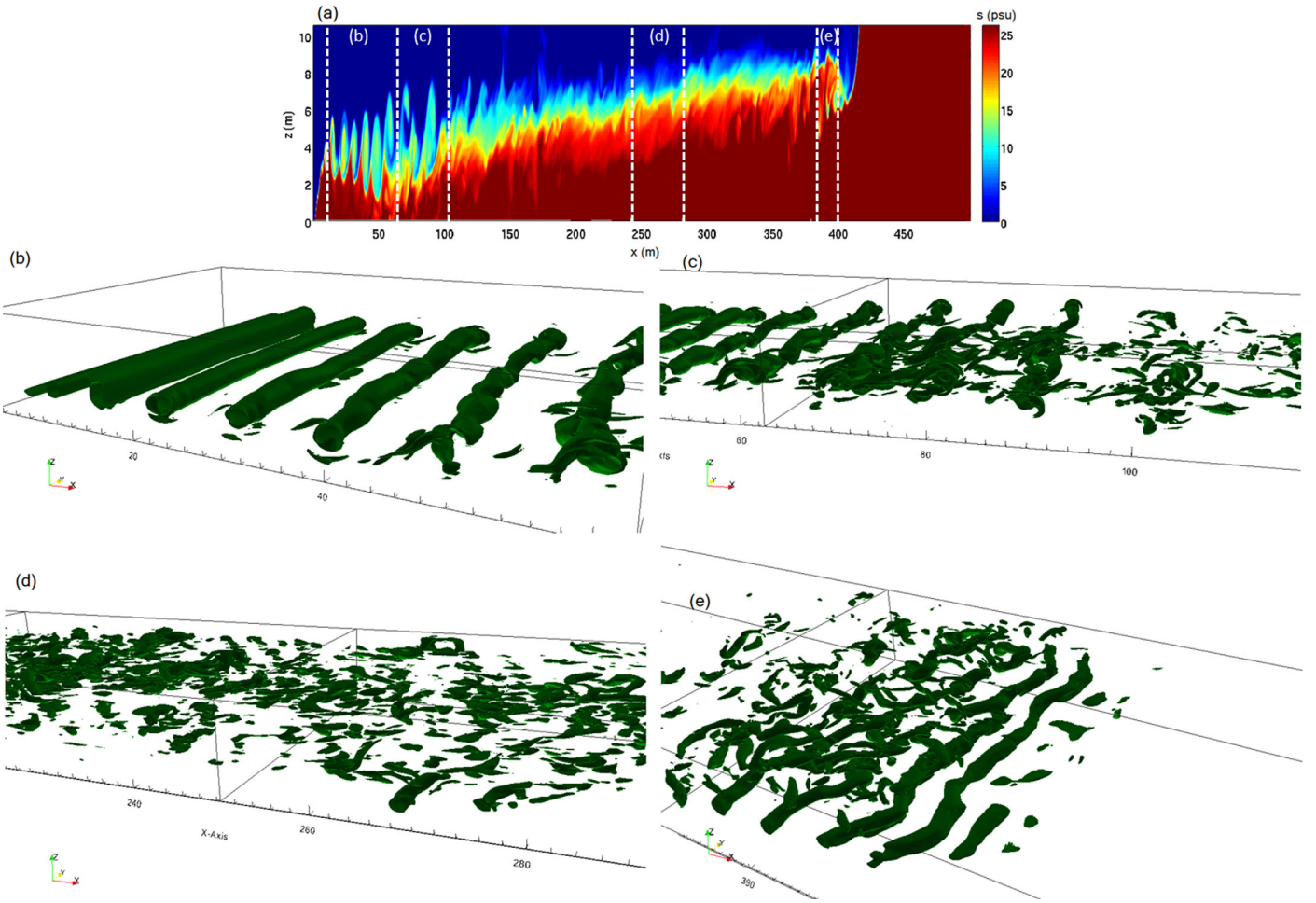


**Figure 5.** (a) Snapshot of salinity distribution (psu) at the center plane (y = 20 m) for Case 2 at t = 350 s. The corresponding coherent structures visualized by Q-method associated with shear instabilities (b) in the region between x = 10 and 60 m with the iso-surface of Q = 0.1 is shown, (c) in the regime between x = 60 and 100 m with Q = 0.1, (d) region between x = 240 and 280 m with Q = 0.0075, and (e) region between x = 380 and 400 m with Q = 0.1.

evolve into turbulence, and coherent structures break into smaller structures with local irregularities in terms of shape and intensity (see Figure 5d). The composite Froude number continues to increase downstream with an averaged value of 1.53. Particularly, between x = 170 and 350 m, shear instabilities have evolved for sufficiently long period of time and approach an equilibrium stage. Therefore, flow structures become less coherent but more random (see Figure 5d). Further downstream (x = 350–420 m), the process is dominated by the head of the density current where 2-D rollers and 3-D rib-structures emerge again. The flow field at the leading edge is mostly 2-D without 3-D instabilities. The pattern of the leading front is consistent with the previous findings about gravity currents over slip boundaries [*Simpson*, 1972; *Britter and Simpson*, 1978; *Härtel et al*., 2000] since the free surface can be considered as close to a slip boundary [*Härtel et al*., 2000]. The evolution pattern of shear instabilities is consistent with the findings reported in *Pham and Sarkar* [2014]. Here we can identify some discrepancies between Case 1 and Case 2 due to resolution. In the high resolution run of Case 2, the nonlinear and turbulent stage starts at about x = 40 m, which is much earlier than that in Case 1 (starts at about x = 80 m) because the high resolution in Case 2 enables more nonlinear effects to be resolved, and thus accelerates the transfer of kinetic energy into turbulent motions.

Similar to section 4.1, mean flow quantities, e.g., mean streamwise velocity and salinity, together with the Richardson numbers, are used to evaluate the resolved shear instabilities and turbulent mixing. Here the mean quantities are obtained by spanwise-averaging over the domain width and streamwise-averaging over a distance of 48 m, which will be shown later to be about three times the characteristic length of the billow in the simulation. Figure 6b shows the spatial distribution of bulk Richardson number $Ri_b$ of Case 2,

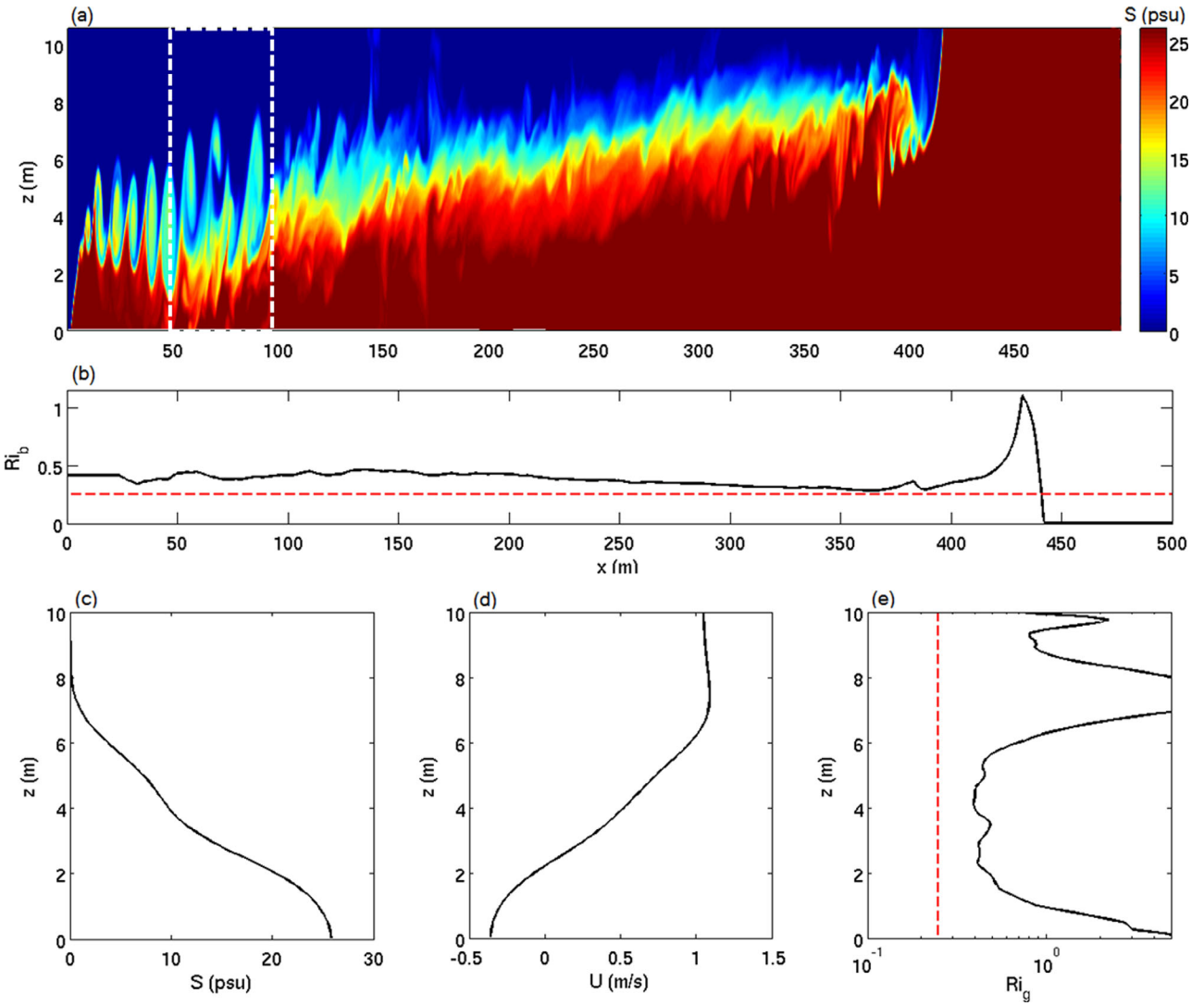


**Figure 6.** (a) Snapshot of salinity distribution at the center plane in the spanwise direction (y = 20 m) in Case 2; (b) streamwise distribution of bulk Richardson number; (c) mean salinity $\langle S \rangle$ (psu); (d) mean streamwise velocity $\langle U \rangle$ (m/s); and (e) gradient Richardson number $Ri_g$ at x = 75 m and at t = 350 s. The white box in Figure 6a indicates the region in the streamwise direction that the mean quantities are averaged over. The red dash line in Figures 6b and 6e represent the value 0.25.

which encompasses the initial growth region (x = 10–100 m), the equilibrium region (x = 100–350 m), and the head region (x = 350–420 m). In the early stage of the growth, high resolution results show larger $Ri_b$ in magnitude, suggesting a more effective conversion of kinetic energy to stratification. However, in the equilibrium region, $Ri_b$ converges to about 0.3, similar to that obtained in low resolution run of Case 1. The simulated evolution process of $Ri_b$ is consistent with that in *Pham and Sarkar* [2014], especially in terms of the equilibrium value of $Ri_b$ at about 0.3.

Figures 6c and 6d show the mean salinity $\langle S \rangle$ and mean flow velocity $\langle U \rangle$ of Case 2 at t = 350 s centered at x = 75 m where the rapid initial growth of shear instabilities were observed (see Figure 5c). The streamwise velocity difference above and below the shear layer is 1.41 m/s, and the thickness of the shear layer is 6.95 m. Figure 6e shows the corresponding vertical profile of gradient Richardson number $Ri_g$ calculated based on the mean flow quantities. Inside the shear layer (z = 1.5–6.4 m), the gradient Richardson number drops to 0.4, while very large $Ri_g$ can be observed outside the shear layer. The characteristics of the mixing process in the equilibrium region centered at x = 250 m are also investigated (see Figure 7). Similar to Figure 6, the mean quantities are calculated by spanwise-averaging over the domain width and streamwise-averaging over about three billows (48 m). At x = 250 m, the streamwise velocity difference is about 1.4 m/s while the shear layer thickness is about 4.7 m, which is smaller than that during the initial growth of shear

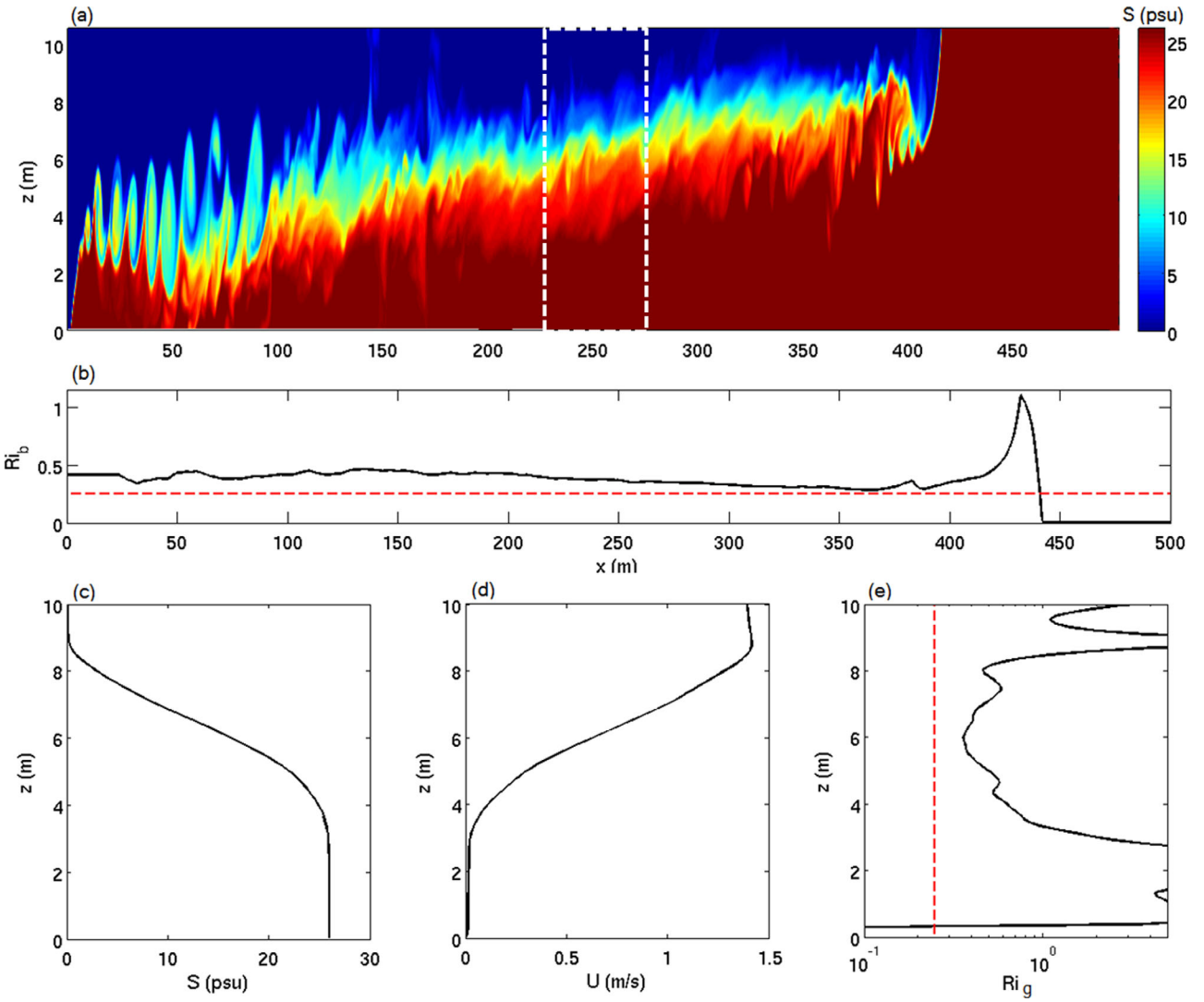


**Figure 7.** (a) Snapshot of salinity distribution at the center plane in the spanwise direction (y = 20 m) in Case 2; (b) streamwise distribution of bulk Richardson number; (c) mean salinity $\langle S \rangle$ (psu); (d) mean streamwise velocity $\langle U \rangle$ (m/s); and (e) gradient Richardson number $Ri_g$ at x = 250 m and at t = 350 s. The white box in Figure 7a indicates the region in the streamwise direction that the mean quantities are averaged over. The red dash line in Figures 7b and 7e represent the value 0.25.

instabilities at x = 75 m. The resulting Reynolds number based on half-depth and half of the velocity difference is around $Re = 1.6 \times 10^6$, which is about three times larger than the observed $Re = 5 \times 10^5$ at Connecticut estuary by *Geyer et al.* [2010]. Since the turbulent and mixing characteristics vary with order of magnitude change in *Re* in fully turbulent flow, the factor 3 difference in Reynolds number can be considered small for qualitative comparison. Figure 7e shows the vertical profile of gradient Richardson number $Ri_g$ calculated based on the mean flow quantities at x = 250 m. Very large $Ri_g$ can be observed outside the shear layer where the mixing is small, but $Ri_g$ is close to 0.3 in the shear layer between 4.0 and 8.2 m. With higher spatial resolution used in Case 2, the fluctuation of $Ri_g$ in the shear layer is less intense compared to that of lower resolution of Case 1. Here the upward mixing and downward mixing are almost equally intense. The gradient Richardson number profile obtained in the present numerical simulation is similar to that observed in the field [*Geyer et al.*, 2010]. A similar pattern of gradient Richardson number has been reported by *Nasr-Azadani et al.* [2016] who carried out direct numerical simulation of turbidity current interacting with complex seafloor topography.

Using the high resolution run, we now examine the resolved turbulent cascade processes in more detail. The size of the billow is estimated by computing the spectral representation of the resolved flow field at t = 350 s. The Fourier transform of the vertical velocity field *w* is used to obtain the discrete spectral representation of the field as

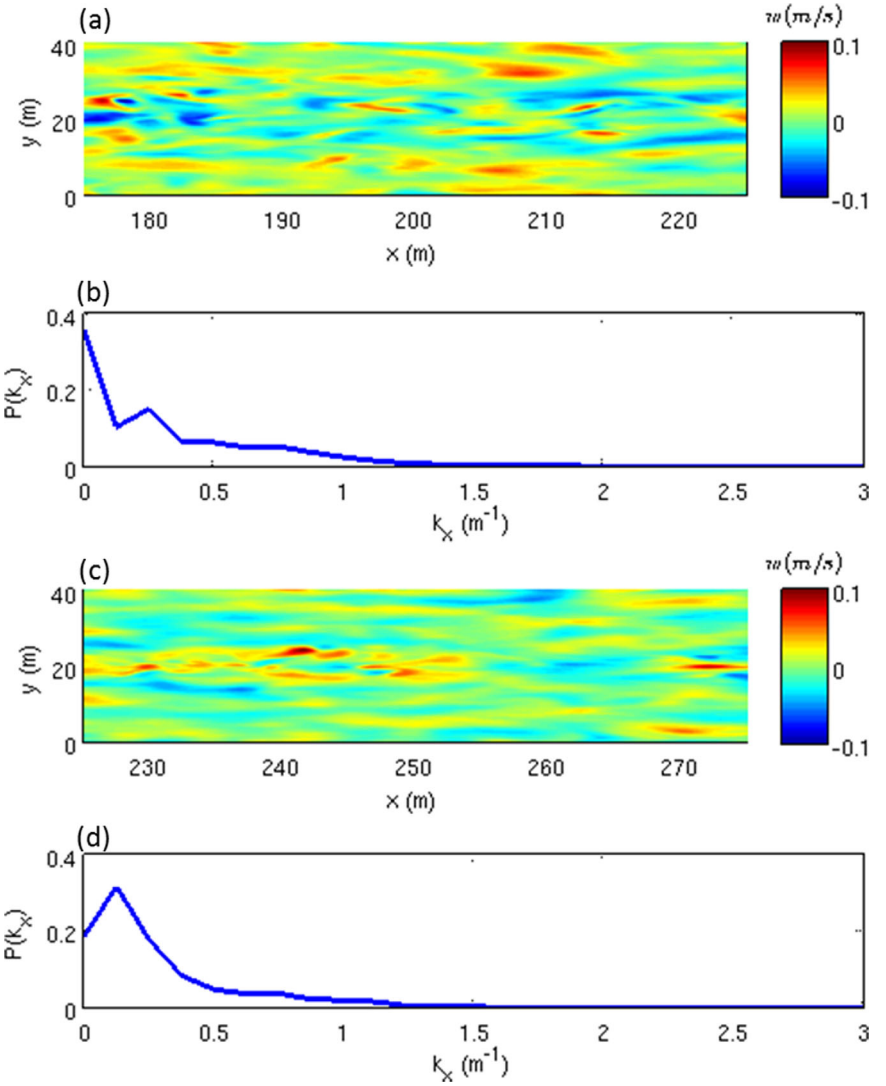


**Figure 8.** (a) Vertical velocity field of Case 2 at t = 350 s at the horizontal plane of z = 5.0 m from x = 175 to 225 m and (b) the corresponding normalized streamwise power spectrum density. (c, d) The corresponding results at the horizontal plane of z = 6.0 m from x = 225 to 275 m.

$$w(x,y,z)=\sum_{n=-N+1}^{N}\hat{w}_n(k_x,y,z)e^{ik_x x} \tag{21}$$

where $k_x$ is the streamwise wavenumber, $\hat{w}_n$ are the Fourier coefficients, and $N=N_x/2$ with $N_x$ as the number of grid points in x direction. The relative importance of various spectral components can be represented by the normalized spanwise power spectral density defined as

$$P(n,z)=\frac{|\hat{w}_n|^2}{\sum_{n=-N+1}^{N}|\hat{w}_n|^2} \tag{22}$$

As a representative example, we select the plane at z = 5.0 m for the region from x = 175 m to x = 225 m (Figure 8a) and z = 6.0 m for the region from x = 225 m to x = 275 m (Figure 8c). In Figure 8a, various scales of coherent structures associated with shear instabilities can be observed. Figure 8b shows the corresponding normalized power spectral density of the vertical velocity. It is clear that the energy is focused between wavenumber $k \approx 0$ (mean flow) and 2 $m^{-1}$, and the averaged wavenumber using the energy as weight is around 0.40 $m^{-1}$ in the region from x = 175 to 225 m, which correspond to the billow sizes around 15.88 m.

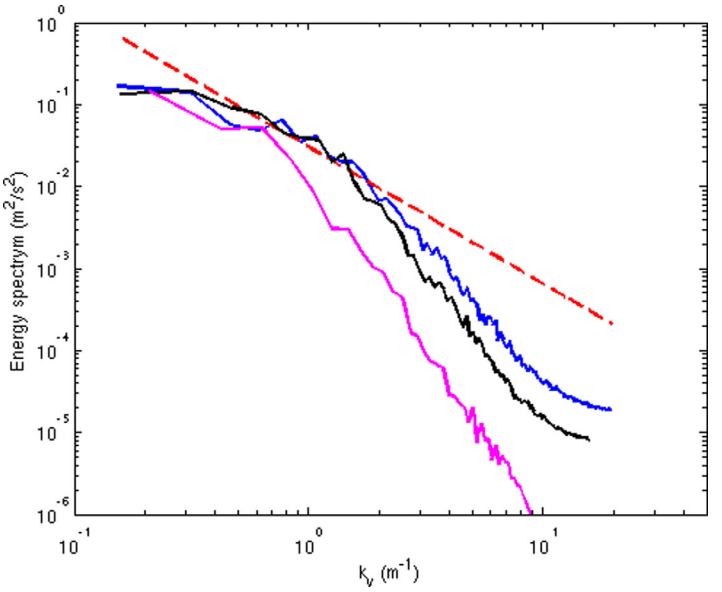


**Figure 9.** Energy spectrum of streamwise velocity in the region between x = 100 m and x = 300 m at t = 350 s from Case 2 (blue line), Case 3 (black line), and Case 1 (magenta line). The red-dashed line represents −5/3 slope.

Similar analysis for region of x = 225–275 m (see Figure 8c) gives the weighted wavenumber of 0.36 $m^{-1}$ and a billow size of 17.60 m. The size of the billow is consistent with the field measured data reported by *Geyer et al*. [2010].

To better evaluate the quality of the present simulation in resolving shear instabilities and turbulence, the energy spectrum of the resolved flow field is presented. Following the Kolmogorov theory in the inertial subrange, the following relationship should hold

$$E(k)=\alpha\varepsilon^{2/3}k^{-5/3} \quad (23)$$

where $E$ is the turbulent kinetic energy spectrum function, $k$ is the wavenumber, $\varepsilon$ is the turbulent dissipation rate, and $\alpha=1.52$ [*Davidson*, 2004; *Pope*, 2000]. According to equation (23), we can see that a successful large-eddy simulation needs to reproduce part of the energy spectrum with −5/3 slope. Figure 9 shows the turbulent kinetic energy spectrum function in the spanwise direction for Case 1, Case 2, and Case 3 averaged over in the region between x = 100 and 300 m where the turbulence is well developed. For Case 2 with the highest resolution ($N_{tot} = 80 \times 10^6$, see Table 1), the energy spectrum between 0.4 $m^{-1}$ (corresponds to the billow size identified before) and 2 $m^{-1}$ shows the expected −5/3 slope, and the spectral width of the resolved energy cascade exceeds 1 order of magnitude. The energy spectrum of Case 3 ($N_{tot} = 40 \times 10^6$, see Table 1) also shows the −5/3 slope, but with a slightly narrower range (0.6–1.6 $m^{-1}$). Case 1 with the lowest resolution barely shows any −5/3 slope in the spectrum and the resolved turbulent energy level is also significantly lower.

Besides examining the spectral slope, turbulent dissipation rate can be estimated for Case 2. One of the ways to estimate turbulent dissipation rate is to use best fit of equation (23) with the Kolmogorov spectrum, which is denoted by $\varepsilon_1$. Using equation (23), the resolved turbulent dissipation rate is estimated to be $\varepsilon_1 = 2\times10^{-3}$ $m^2/s^3$, which is slightly larger than the measured dissipation rate reported by *Geyer et al*. [2010] (around $0.8\times10^{-4}$ to $6.8\times10^{-4}$ $m^2/s^3$ in the braid mixing zone). Larger turbulence dissipation rate in the model may be due to the larger velocity difference across the shear layer, which results in a stronger flow forcing and higher *Re*.

As demonstrated in *Pham and Sarkar* [2014], turbulent dissipation rate can also be estimated from the resolved and parameterized (subgrid) flow field. According to *Pham and Sarkar* [2014], the resolved dissipation rate $\varepsilon_r$ is calculated as

$$\varepsilon_r = 2\nu\langle \bar{S}'_{ij}\bar{S}'_{ij}\rangle \quad (24)$$

and the subgrid dissipation rate $\varepsilon_{sgs}$ is defined as

$$\varepsilon_{sgs} = -\langle S'_{\tau,\ ij}\frac{\partial \bar{u}_i{}'}{\partial x_j}\rangle \quad (25)$$

In Case 2, consistent with the large-eddy simulation study of *Pham and Sarkar* [2014], we obtain $\varepsilon_{sgs}$ that is significantly larger than $\varepsilon_r$. Hence, $\varepsilon_{sgs}$ is used here to estimate total dissipation rate approximately. The distribution of $\varepsilon_{sgs}$ can be seen in Figure 10a. The value of $\varepsilon_{sgs}$ approaches $5\times10^{-4}$ $m^2/s^3$ in the head region and is about $1.0\times10^{-4}$ $m^2/s^3$ at the braids of the billows in the equilibrium region. These values are slightly smaller than those estimated using energy spectrum but consistent with the field data reported by *Geyer et al*. [2010].

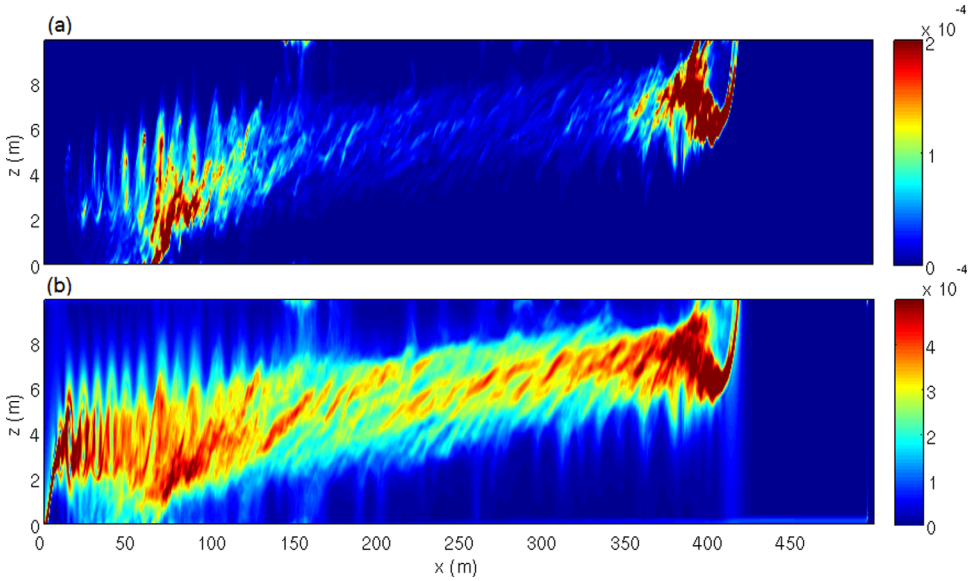


**Figure 10.** Snapshots of spanwise-averaged (a) subgrid dissipation rate $\varepsilon_{sgs}$ ($m^2/s^3$) and (b) subgrid-scale viscosity $\nu_{sgs}$ ($m^2/s$) at t = 350 s of Case 2.

To further inspect the resolved turbulent kinetic energy spectrum, subgrid dissipation rate $\varepsilon_{sgs}$, together with the subgrid viscosity $\nu_{sgs}$, are used to estimate the demarcation length scale $l_{DI}$ which separates the universal equilibrium range into the inertial subrange and the dissipation range [*Pope*, 2000], i.e., a length scale at which the energy spectrum should start to deviate from the −5/3 slope. According to *Pope* [2000], $l_{DI}$ is estimated to be

$$l_{DI}=60\eta=60\left(\frac{\nu^3}{\varepsilon}\right)^{1/4} \tag{26}$$

where $\eta$ is the Kolmogorov length scale. Here using the analogy to equation (26), $l_{DI}$ can be evaluated based on $\nu_{sgs}$ and $\varepsilon_{sgs}$:

$$l_{DI}\approx 60\left(\frac{{\nu_{sgs}}^3}{\varepsilon_{sgs}}\right)^{1/4} \tag{27}$$

Distribution of $\nu_{sgs}$ is shown in Figure 10b. Using the present standard Smagorinsky closure, $\nu_{sgs}$ is about $3 \times 10^{-4}$ to $5 \times 10^{-4}$ $m^2/s$ in the braids of the equilibrium region. In the head region, $\nu_{sgs}$ can approach $1 \times 10^{-3}$ $m^2/s$. The value of $l_{DI}$ in the braid mixing zone can be estimated to be around 3 m, which corresponds to about $k_y = 2$ $m^{-1}$ in Figure 9 where the energy spectrum of Case 1 starts to deviate from the −5/3 slope.

In summary, high resolution run (Case 2) with grid size similar to the estimated Ozmidov length scale reproduces expected shear layer characteristics in terms of bulk Richardson number and gradient Richardson number. The resolved average length scale of billows is about 16 m, which is close to field observed values. Moreover, the resolved spectrum encompasses about 1 order of magnitude of turbulent energy cascade and the spectrum behavior is demonstrated to be self-consistent using the estimated turbulent dissipation rate and computed subgrid viscosity. Although the present grid resolution is lower than the large-eddy simulation for shear instabilities of *Pham and Sarkar* [2014], which has a grid size about three times smaller than the Ozmidov length scale, our simulation can still produce several key features of stratified shear layer and bulk behavior of the density current.

## 5. Discussion

### 5.1. Comparison With Broadband Acoustic Backscatter Measurement

As discussed previously, field observations of Connecticut River plume using a broadband acoustic backscatter technique show that shear instabilities have distinctive characteristics, with high turbulent fluctuations appearing in the braids, not in the core [*Geyer et al.*, 2010]. The purpose of this subsection is to

examine whether the present numerical simulation (Case 2) can reproduce such features and to indicate which flow quantities in the model can be used to represent instantaneous turbulence field similar to measured acoustic backscatter signals. Based on the same field data of *Geyer et al*. [2010], *Lavery et al*. [2013] suggested that the measured acoustic backscatter signal can be associated with turbulent salinity microstructure. The acoustic frequencies used in the measurement extend over wavenumbers in the viscous-convective subrange in this environment. In the present numerical simulation, we can only resolve the wavenumber up to O(10) $m^{-1}$. Therefore, it is difficult to get the same range of scales obtained from the field measurements. However, according to the subgrid-scale closure methodology adopted here, we can estimate the subgrid-scale turbulent production of salinity fluctuations, which is temporally and spatially correlated with the turbulent salinity microstructure. Since the Smagorinsky viscosity is adopted to parameterize the subgrid stress in this study, the turbulent production of salinity fluctuations at subgrid scale is estimated as

$$P_s = \left(\nu + \nu_{sgs}\right)\left(\frac{\partial s}{\partial z}\right)^2 \tag{28}$$

Figures 11b and 12b show the production of salinity fluctuations at subgrid scale of Case 2 for a 50 m segment in the initial growth region and in the equilibrium region at t = 350 s, respectively. The high intensity of subgrid turbulent production of salinity fluctuation occurs at the braids, which is consistent with the field observation [see *Geyer et al*., 2010, Figure 2]. Besides the production of salinity fluctuation, several other quantities computed from the simulation results are also used to represent turbulence in shear instabilities. Figures 11c and 12c show the subgrid-scale dissipation rate $\varepsilon_{sgs}$, while Figures 11d and 12d show the spanwise component of vorticity $\omega_y$, respectively. We observe that similar to $P_s$, the highest subgrid-scale dissipation rate $\varepsilon_{sgs}$ also occurs along the braids in the present simulation. However, high value of vorticity $\omega_y$ also shows up at the cores in the initial growth region (see the first two billows in the left portion of Figure 11d). During the initial growth of instabilities, region of high flow shear causes the observed large $\omega_y$, however, it may take longer time to evolve into highly fluctuating turbulent flow. In the equilibrium stage, regions of high $\omega_y$ become consistent with the distribution of $P_s$ and $\varepsilon_{sgs}$ (see Figure 12).

In the realistic river mouth regimes, due to channel expansion and acceleration of the river plume [*Chen et al*., 2009; *Hetland*, 2008; *MacDonald and Geyer*, 2004], the forcing of shear instabilities can persist strong for a long distance as observed in *Geyer et al*. [2010]. In the present study, lateral channel expansion is not included. As a result, the shear instabilities would be expected to be more persistent in a spreading river plume than in the simulation shown here. Moreover, the coherent 2-D rollers near the inlet boundary may not be observed in reality because there are many sources of random perturbations in the field. If lateral channel expansion were simulated, the gradient Richardson number would be expected to be lower (perhaps just below 0.25) due to the persistent straining of the interface, with less along-flow variability.

### 5.2. Surface Signatures

As discussed in section 4.1, the predicted surface signatures can be compared with remote sensing imagery to understand the water column processes associated with particular types of surface signatures. Results of Case 2 provide an opportunity to study the correspondence between the surface velocity divergence and fronts and shear instabilities generated in the water column (see Figure 15). The most obvious surface signature shown in Figure 15a is the density current front located at x = 420 m, which is represented by a narrow region of surface velocity convergence (see the blue strip). Moreover, notable velocity divergence can be observed at the lift-off region (see the yellow strip in x = 5–10 m in Figure 13a), which is due to the head of the stationary density current at the bottom. Similar surface signatures have been observed in the X-radar measurement during the flood tide condition at Mouth of Columbia River [*Honegger*, 2015].

Besides the front of density currents, surface signatures associated with shear instabilities can also be identified. For example, in the region from x = 140 m to x = 175 m, several patches of irregular surface signatures associated with the shear instabilities can be seen. According to the surface salinity plot in Figure 13b and cross-sectional view (at the plane of y = 5 m) in Figure 13c, it is clear that saltier water is entrained to the surface between x = 150 m and x = 166 m due to shear instabilities (note the range of salinity in Figure 13b is only between 0 and 3 psu). Inspecting the vertical salinity distribution at the center plane y = 20 m (see Figure 13d), another two spots of salinity entrainment at x = 140 and 175 m can be identified. Because of

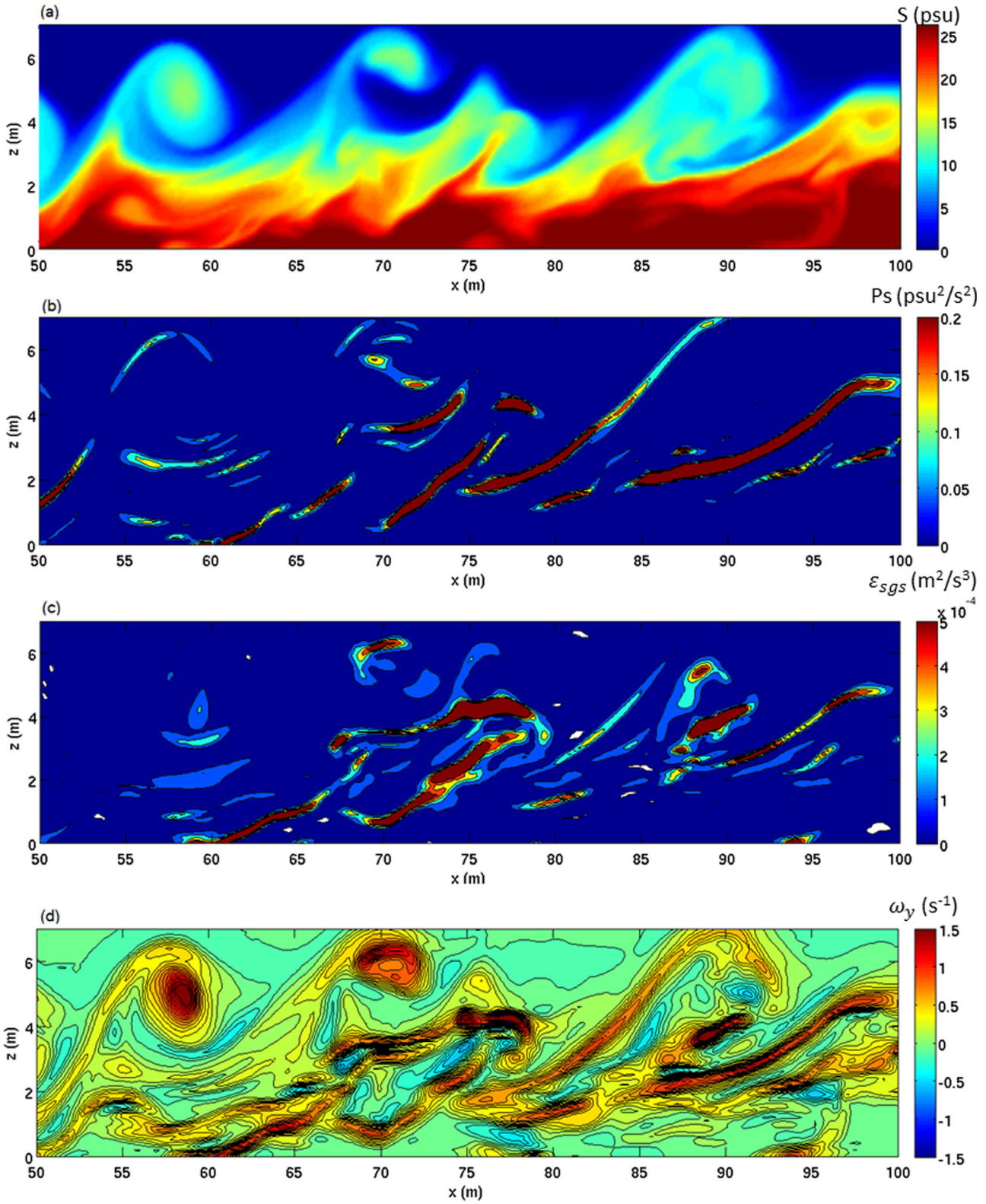


**Figure 11.** Snapshots of Case 2 at t = 350 s for (a) salinity (psu), (b) subgrid production of salinity fluctuation ($psu^2/s^2$), (c) subgrid dissipation rate $\varepsilon_{sgs}$ ($m^2/s^3$), and (d) spanwise vorticity $\omega_y$ ($s^{-1}$) at the center plane from x = 50 to 100 m.

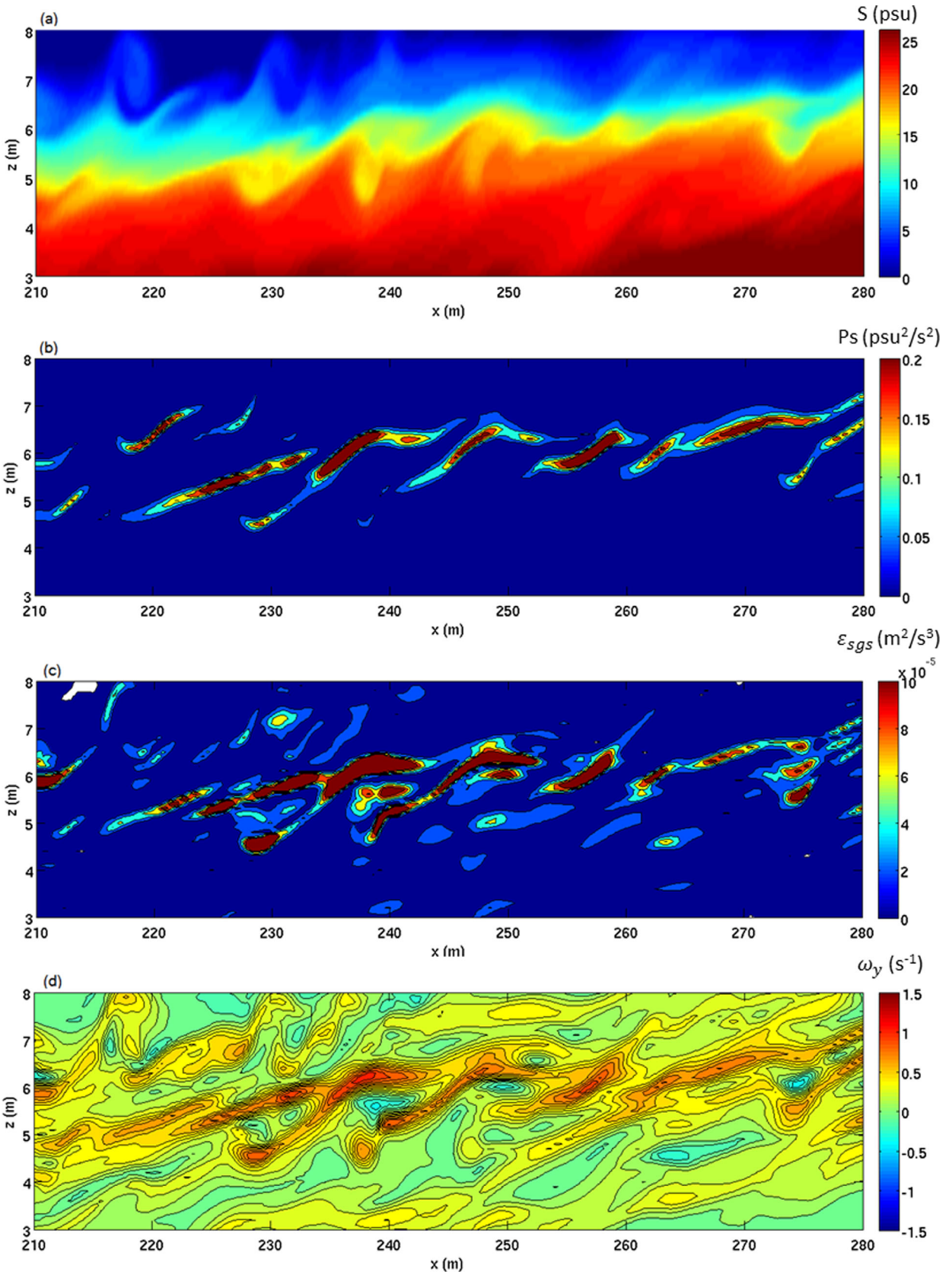


**Figure 12.** Snapshots of Case 2 at t = 350 s for (a) salinity (psu), (b) subgrid production of salinity fluctuation (psu$^2$/s$^2$), (c) subgrid dissipation rate $\varepsilon_{sgs}$ (m$^2$/s$^3$), and (d) spanwise vorticity $\omega_y$ (s$^{-1}$) at the center plane from x = 210 to 280 m.

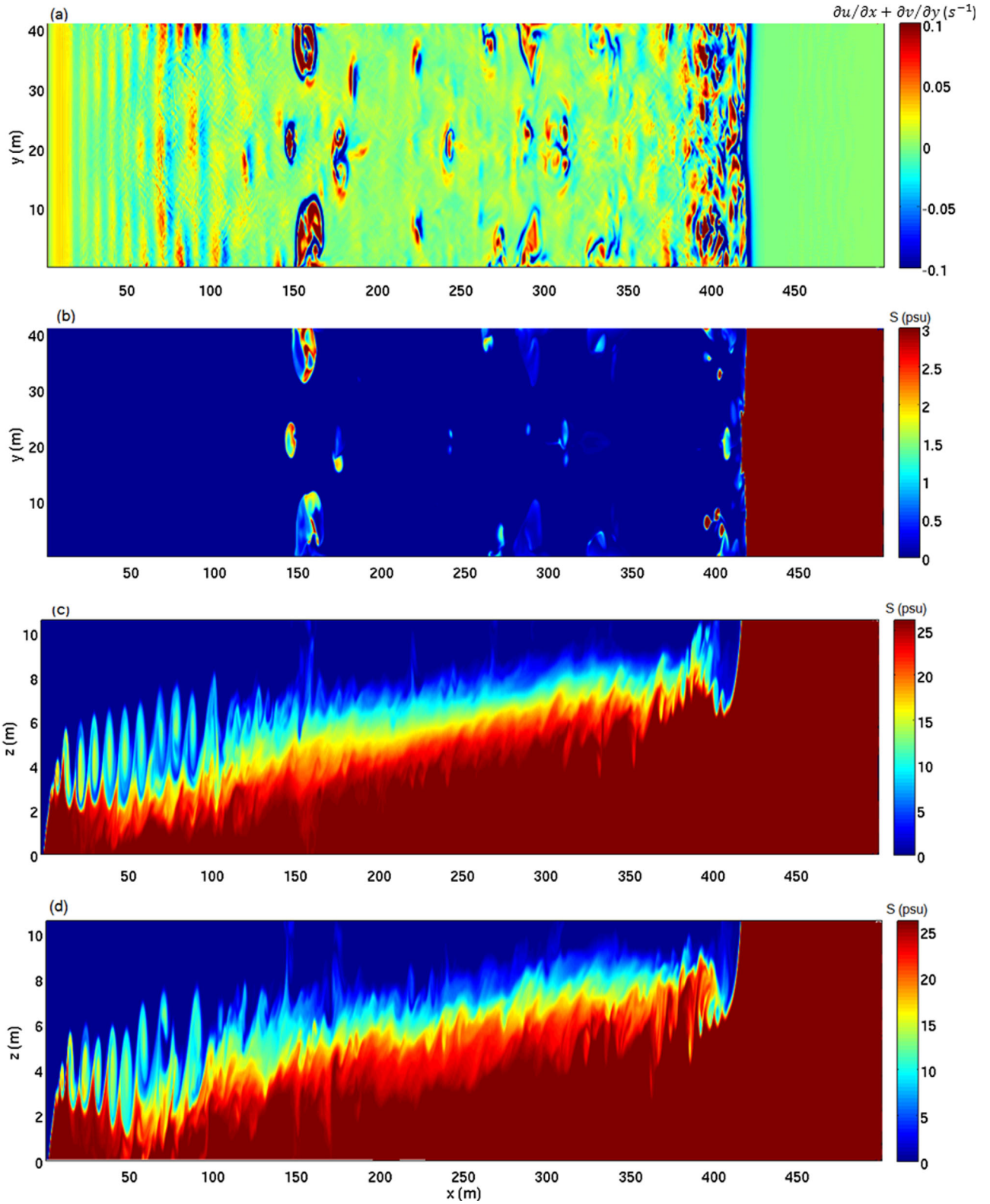


**Figure 13.** Snapshots of Case 2 at t = 350 s for (a) the surface horizontal velocity divergence ($s^{-1}$), (b) salinity distribution at the free surface, (c) salinity distribution at the plane of y = 5 m, and (d) the plane of y = 20 m.

the large layer depth, some shear instabilities cannot entrain sufficient saline water to reach the surface (see the two patches at x = 225 m). However, surface signatures through horizontal velocity divergence are still noticeable. Similar condition can also be found at several other locations (e.g., in the transitional zone x = 50–100 m). It appears that surface velocity divergence is an effective identifier for the water column processes.

### 5.3. A Note on Grid Resolution and Subgrid Turbulence Closure

As demonstrated in section 4.2, for the highest resolution simulation (Case 2) where the grid size is similar to the Ozmidov length scale, turbulent dissipation rate can be approximately calculated by the subgrid turbulent dissipation rate $\varepsilon_{sgs}$ (see equation (25)). In many field-scale applications, we expect the resolution can be lower than that used in Case 2. In this situation, the resolved dissipation rate $\varepsilon_r$ (see equation (24)) is certainly negligible. However, the key issue to be investigated is whether the modeled subgrid dissipation rate

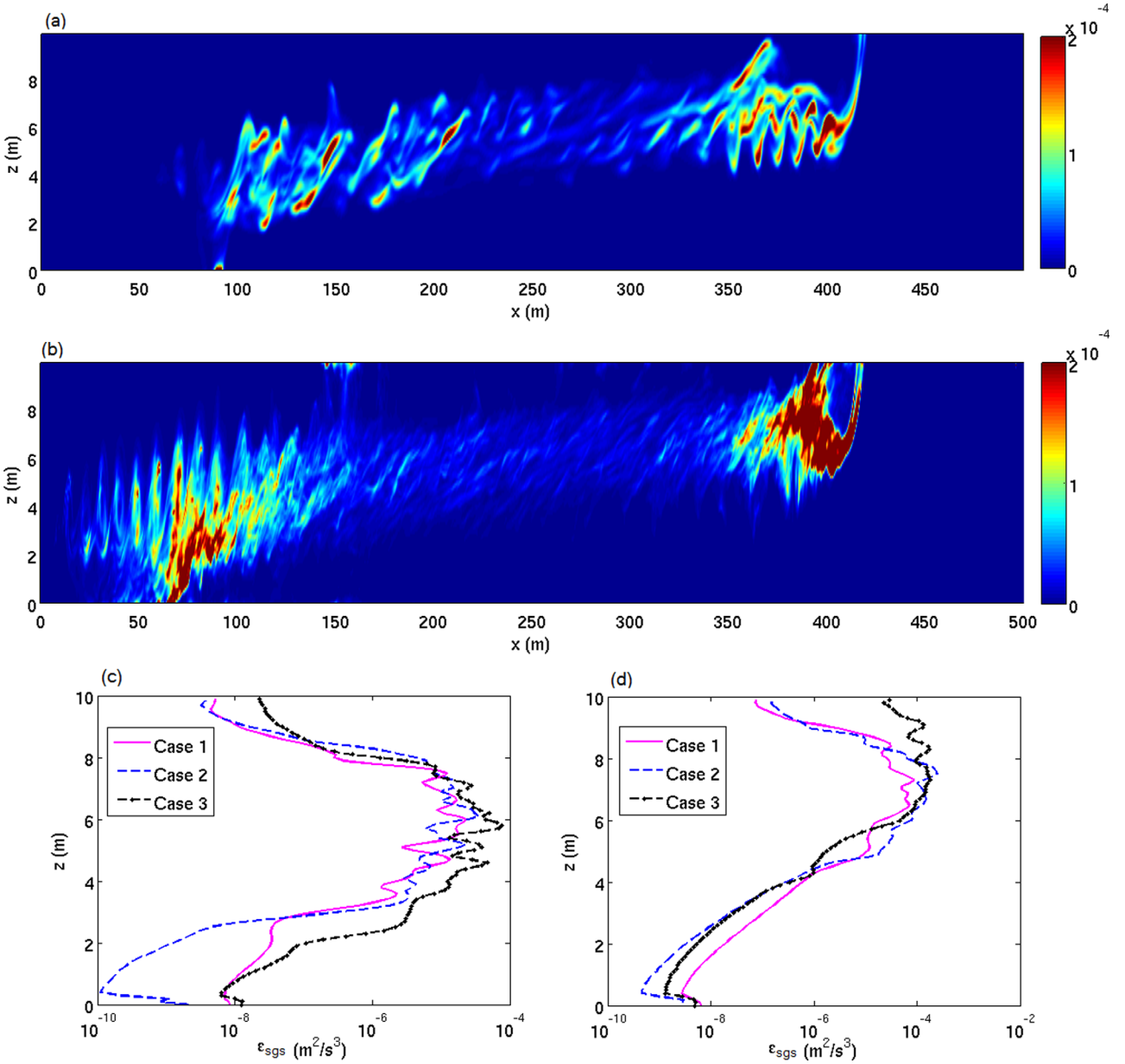


**Figure 14.** Snapshots of spanwise-averaged subgrid dissipation rate $\varepsilon_{sgs}$ ($m^2/s^3$) of (a) Case 1 and (b) Case 2. Vertical profile of subgrid dissipation rate for Cases 1–3 at x = 250 m in the equilibrium region and x = 375 m in the head region are shown in Figures 14c and 14d.

$\varepsilon_{sgs}$ is still meaningful and can be used to estimate turbulent dissipation rate. Snapshots of spanwise-averaged subgrid dissipation rate for the entire density current between the high resolution Case 2 and low resolution Case 1 are presented in Figures 14a and 14b. We can observe that the subgrid dissipation rate calculated by low resolution (Case 1) also shows similar structure with higher magnitude in the head region than that in the equilibrium region. Major difference is observed near the lift-off region of the density current where the flow is in the transitional state. However, the predicted subgrid dissipation rate in the equilibrium region and in the head region appears to be on the same order of magnitude between these two cases. In Figures 14c and 14d, vertical profiles of subgrid dissipation rate in the equilibrium region (x = 250 m) and head region (x = 375 m) for Cases 1–3 are presented. Inside the shear layer, the lowest resolution run (Case 1) under predicts the subgrid dissipation rate by about factor 2 comparing to the highest resolution run (Case 2). Moreover, the intermediate resolution run (Case 3) predicts somewhat higher (also within factor two) subgrid dissipation rate than that of Case 2. In the head region (Figure 14d), the lowest resolution run (Case 1) predicts a subgrid turbulent dissipation that is within factor three lower than that of two higher resolution runs. In summary, the predicted $\varepsilon_{sgs}$ values are not very sensitive to three sets of resolution studied here.

The numerical results presented here show that the bulk properties of the shear layer can be predicted reasonably well in the low resolution run (Case 1) where the grid size is several times larger than the Ozmidov length scale. However, we should note that according to our numerical experiments, the vertical resolution across the shear layer is the most essential. When the vertical grid size is increased by a factor two, the predicted shear layer properties in the equilibrium region become incorrect and the braids of billows can barely be resolved. Moreover, the predicted subgrid turbulent dissipation rate in the equilibrium region becomes several orders of magnitude lower. Lessons learned in this study in resolving shear instabilities can provide useful guidelines to further simulate more complex problems requiring larger domains, such as river plumes and the formation of complex frontal features [e.g., *O'Donnell et al*., 2008; *Horner-Devine et al*., 2013]. For example, according to measured turbulence characteristic in the frontal region of the Connecticut River plume, the Ozmidov scale is about 0.5 m, the characteristic width of the front zone is about 15 m while the overall model domain to encompass the plume and a cross current in Long Island Sound is at least 5 km. A quick estimate suggests that using about $100 \times 10^6$ grid points with the foremost consideration in the vertical grid resolution in the water column, it is possible to achieve a vertical grid size of about 0.1 m and a horizontal grid size a few times larger than the Ozmidov scale. However, detailed model validation with measured frontal zone characteristics and turbulence statistics are necessary to ensure such modeling proposition is appropriate.

Finally, the effect of subgrid Smagorinsky viscosity is essential in the present high resolution runs (Cases 2 and 3). A numerical experiment identical to the highest resolution Case 2 but setting $\nu_{sgs}=0$ suggests that ignoring the Smagorinsky viscosity give incorrect results in the head region. The resolved flow field in the head region shows very intense fluctuations and the front eventually splits into two at about t = 200 s. Such unrealistic fluctuations may eventually lead to numerical instability. This finding confirms our speculation that in Case 1 of low resolution, the resolved flow field is also affected by numerical dissipation/diffusion. However, when the resolution is significantly increased, numerical dissipation/diffusion becomes much smaller than the subgrid Smagorinsky viscosity and the parameterization of subgrid viscosity plays a key role in the accuracy of the resolved flows. Therefore, future work should focus on a more sophisticated dynamic procedure in the Smagorinsky closure in high resolution simulations.

## 6. Conclusion

The 3-D $\sigma$-coordinate nonhydrostatic model NHwave is applied to study the structure of an idealized density current in the field scale with the Reynolds number of the resolved shear instability exceeding $1.6\times10^6$. With spatial resolution close to the Ozmidov length scale, the model successfully predicted the bulk properties of shear instabilities, such as the size of billows, turbulent dissipation rate, and results are comparable to the field observation reported by *Geyer et al*. [2010]. Furthermore, model results also indicate that the production of salinity fluctuation is similar to the measured salinity turbulent microstructures obtained via acoustical backscatter intensity with high turbulence mainly populated in the braids. Both the spanwise vorticity of the resolved flow field and the subgrid turbulent dissipation rate can also be used to identify the

structure of the resolve shear instabilities. The simulation results also provide the surface signatures, which enables us to link the surface signature, represented by the horizontal divergence of velocity at the surface, with the turbulence billows and fronts underneath. Finally, subgrid Smagorinsky viscosity plays a key role in the validity of the present simulation, particularly in high numerical resolution.

**Acknowledgments**
This work is supported by Office of Naval Research (N00014-15-1-2612 and N00014-16-1-2948) and National Science Foundation (OCE-1334325 and OCE-1232928). We thank one of the main developers of NHWAVE, Gangfeng Ma, for providing useful comments and an anonymous reviewer's thorough comments that improves the manuscript. Simulations presented in this paper are carried out on Extreme Science and Engineering Discovery Environment (XSEDE) SuperMIC (TG-OCE100015) and on University of Delaware community clusters, Mills and Farber. The data for this paper can be obtained freely by contacting the lead author at zzhou@udel.edu.

## References

Atsavapranee, P., and M. Gharib (1997), Structures in stratified plane mixing layers and the effects of cross-shear, *J. Fluid Mech.*, *342*, 53–86.
Britter, R. E., and J. E. Simpson (1978), Experiments on the dynamics of a gravity current head. *J. Fluid Mech.*, *88*(2), 223–240.
Caulfield, C. P., S. Yoshida, and W. R. Peltier (1996), Secondary instability and three dimensionalization in a laboratory accelerating shear layer with varying density differences, *Dyn. Atmos. Oceans*, *23*, 125–138.
Chen, F., D. G. MacDonald, and R. D. Hetland (2009), Lateral spreading of a near-field river plume: Observations and numerical simulations, *J. Geophys. Res.*, *114*, C07013, doi:10.1029/2008JC004893.
Chickadel, C. C., A. R. Horner-Devine, S. A. Talke, and A. T. Jessup (2009), Vertical boil propagation from a submerged estuarine sill, *Geophys. Res. Lett.*, *36*, L10601, doi:10.1029/2009GL037278.
Chickadel, C. C., S. A. Talke, A. R. Horner-Devine, and A. T. Jessup (2011), Infrared-based measurements of velocity, turbulent kinetic energy, and dissipation at the water surface in a tidal river, *IEEE Geosci. Remote Sens. Lett.*, *8*(5), 849–853.
Corcos, G. M., and F. S. Sherman (1976), Vorticity concentration and the dynamics of unstable free shear layers, *J. Fluid Mech.*, *73*(2), 241–264.
Davidson, P. A. (2004), *Turbulence: An Introduction for Scientists and Engineers*, Oxford Univ. Press, New York.
Derakhti, M., J. T. Kirby, F. Shi, and G. Ma (2016), NHWAVE: Consistent boundary conditions and turbulence modeling, *Ocean Modell.*, *106*, 121–130, doi:10.1016/j.ocemod.2016.09.002.
Elias, E. P. L., G. Gelfenbaum, and A. J. V. der Westhuysen (2012), Validation of a coupled water-flow model in a high-energy setting: The mouth of the Columbia River, *J. Geophys. Res.*, *117*, C09011, doi:10.1029/2012JC008105.
Fringer, O. B., M. Gerritsen, and R. L. Street (2006), An unstructured-grid, finite-volume, nonhydrostatic, parallel coastal ocean simulator, *Ocean Modell.*, *14*, 139–173.
Garcia, M. H. (1993), Hydraulic jumps in sediment-driven bottom currents, *J. Hydraul. Eng.*, *119*, 1094–1117.
Garvine, R. W. (1974) Dynamics of small-scale oceanic fronts, *J. Phys. Oceanogr.*, *4*, 557–569.
Garvine, R. W. (1975), The distribution of salinity and temperature in the Connecticut River estuary, *J. Geophys. Res.*, *80*(9), 1176–1183.
Garvine, R. W., and J. D. Monk (1974), Frontal structure of a river plume, *J. Geophys. Res.*, *79*(15), 2251–2259.
Geyer, W. R., A. C. Lavery, M. E. Scully, and J. H. Trowbridge (2010), Mixing by shear instability at high 'Reynolds' number, *Geophys. Res. Lett.*, *37*, L22607, doi:10.1029/2010GL045272.
Giddings, S. N., D. A. Fong, S. G. Monismith, C. C. Chickadel, K. A. Edwards, W. J. Plant, B. Wang, O. B. Fringer, A. R. Horner-Devine, and A. T. Jessup (2012), Frontogenesis and frontal progression of a trapping-generated estuarine convergence front and its influence on mixing and stratification, *Estuaries Coasts*, *35*(2), 665–681.
Gottlieb, S., C.-W. Shu, and E. Tadmor (2001), Strong stability-preserving high-order time discretization methods, *SIAM Rev.*, *43*, 89–112.
Härtel, C., E. Meiburg, and F. Necker (2000), Analysis and direct numerical simulation of the flow at a gravity-current head. Part 1. Flow topology and front speed for slip and no-slip boundaries, *J. Fluid Mech.*, *418*, 189–212.
Hetland, R. D. (2008), Spreading in the near-field Merrimack river plume, *Ocean Modell.*, *21*(1–2), 12–21.
Honegger, D. A. (2015), Depth estimation and frontal imaging via X-band marine radar, PhD thesis, Oreg. State Univ., Corvallis.
Horner-Devine, A. R., C. C. Chickadel, and D. G. MacDonald (2013), Coherent structures and mixing at a river plume front, in *Coherent Flow Structures at Earth's Surface*, 1st ed., edited by J. G. Venditti et al., Wiley-Blackwell, John Wiley and Sons, River Street, N. J.
Ilicak, M., T. M. Özgökmen, H. Peters, H. Z., Baumert, and M. Iskandarani (2008), Performance of two-equation turbulence closures in three-dimensional simulations of the Red Sea overflow, *Ocean Modell.*, *24*(3), 122–139.
Jeong, J., and F. Hussain (1995), On the identification of a vortex, *J. Fluid Mech.*, *285*, 69–94.
Koop, C. G., and F. K. Browand (1979), Instability and turbulence in a stratified fluid with shear, *J. Fluid Mech.*, *93*, 135–159.
Lai, Z., C. Chen, G. W. Cowles, and R. C. Beardsley (2010), A nonhydrostatic version of FVCOM: 2. Mechanistic study of tidally generated nonlinear internal waves in Massachusetts Bay, *J. Geophys. Res.*, *115*, C12049, doi:10.1029/2010JC006331.
Lavery, A. C., W. R. Geyer, and M. E. Scully (2013), Broadband acoustic quantification of stratified turbulence, *J. Acoust. Soc. Am.*, *134*(1), 40–54.
Ma, G., F. Shi, and J. T. Kirby (2012), Shock-capturing non-hydrostatic model for fully dispersive surface wave processes, *Ocean Modell.*, *43–44*, 22–35.
Ma, G., J. T. Kirby, and F. Shi (2013), Numerical simulation of tsunami waves generated by deformable submarine landslides, *Ocean Modell.*, *69*, 146–165.
MacDonald, D. G., and W. R. Geyer (2004), Turbulent energy production and entrainment at highly stratified estuarine front, *J. Geophys. Res.*, *109*, C05004, doi:10.1029/2003JC002094.
Marshall, J., C. Hill, L. Perelman, C. Heisey, and A. Adcroft (1997), Hydrostatic, quasi-hydrostatic and nonhydrostatic ocean modeling, *J. Geophys. Res.*, *102*(C3), 5733–5752.
Mashayek, A., and W. R. Peltier (2011), Three dimensionalization of the stratified mixing layer at high Reynolds number, *Phys. Fluids*, *23*, 111701.
Mashayek, A., and W. R. Peltier (2012a), The 'zoo' of secondary instabilities precursory to stratified shear flow transition; Part 1. Shear aligned convection, paring, and braid instabilities, *J. Fluid Mech.*, *708*, 5–44.
Mashayek, A., and W. R. Peltier (2012b), The 'zoo' of secondary instabilities precursory to stratified shear flow transition: Part 2. The influence of stratification, *J. Fluid Mech.*, *708*, 45–70.
Mashayek, A., and W. R. Peltier (2013), Shear-induced mixing in geophysical flows: Does the route to turbulence matter to its efficiency, *J. Fluid Mech.*, *725*, 216–261.
Masunaga, E., H. Homma, H. Yamazaki, O. B. Fringer, T. Nagai, Y. Kitade, and A. Okayasu (2015), Mixing and sediment resuspension associated with internal bores in a shallow bay, *Cont. Shelf Res.*, *110*, 85–99.
Meneveau, C., and J. Katz (2000), Scale-invariance and turbulence models for large-eddy simulation, *Annu. Rev. Fluid Mech.*, *32*, 1–32.
Nash, J. D., and J. N. Moum (2005), River plumes as a source of large-amplitude internal waves in the coastal ocean, *Nature*, *437*, 400–403.

Nash, J. D., L. F. Kilcher, and J. N. Moum (2009), Structure and composition of a strongly stratified, tidally pulsed river plume, *J. Geophys. Res.*, *114*, C00B12, doi:10.1029/2008JC005036.
Nasr-Azadani, M. M., E. Meiburg, and B. Kneller (2016), Mixing dynamics of turbidity currents interacting with complex seafloor topography, *Environ. Fluid Mech.*, 1–23.
O'Donnell, J. (1990) The formation and fate of a river plume: A numerical model, *J. Phys. Oceanogr.*, *20*, 551–569.
O'Donnell, J., S. G. Ackleson, and E. R. Levine (2008), On the spatial scales of a river plume, *J. Geophys. Res.*, *113*, C04017, doi:10.1029/2007JC004440.
Orton, P. M., and D. A. Jay (2005), Observations at the tidal plume front of a high volume river outflow, *Geophys. Res. Lett.*, *32*, L11605, doi:10.1029/2005GL022372.
Pham, H. T., and S. Sarkar (2014), Large eddy simulations of a stratified shear layer, *J. Fluids Eng.*, *136*(6), 060913.
Plant, W. J., et al. (2009), Remotely sensed river surface features compared with modeling and in situ measurements, *J. Geophys. Res.*, *114*, C11002, doi:10.1029/2009JC005440.
Plant, W. J., W. C. Keller, K. Hayes, and G. Chatham (2010a), Normalized radar cross section of the sea backscatter: 1. Mean levels, *J. Geophys. Res.*, *115*, C09032, doi:10.1029/2009JC006078.
Plant, W. J., W. C. Keller, K. Hayes, G. Chatham, and N. Lederer (2010b), Normalized radar cross section of the sea for backscatter: 2. Modulation by internal waves, *J. Geophys. Res.*, *115*, C09033, doi:10.1029/2009JC006079.
Pope, S. B. (2000), *Turbulent Flows*, Cambridge Univ. Press, New York.
Ralston, D. K., W. R. Geyer, J. A. Lerczak, and M. Scully (2010), Turbulent mixing in a strongly forced salt wedge estuary, *J. Geophys. Res.*, *115*, C12024, doi:10.1029/2009JC006061.
Scotti, A. (2008), A numerical study of the frontal region of gravity currents propagating on a free-slip boundary, *Theor. Comput. Fluid Dyn.*, *22*(5), 383–402.
Scully, M. E., W. R. Geyer, and J. H. Trowbridge (2011), The influence of stratification and non-local turbulent production on estuarine turbulence: An assessment of turbulence closure with field observations, *J. Phys. Oceanogr.*, *41*, 166–185.
Shi, F., C. Chickadel, T.-J. Hsu, J. T. Kirby, G. Farquharson, and G. Ma (2017), High-resolution non-hydrostatic modeling of frontal features in the mouth of the Columbia River, *Estuaries Coasts*, *40*, 296–309, doi:10.1007/s12237-016-0132-y.
Simpson, J. E. (1972), Effects of the lower boundary on the head of a gravity current, *J. Fluid Mech.*, *53*(4), 759–768.
Simpson, J. E. (1982), Gravity currents in the laboratory, atmosphere, and ocean, *Annu. Rev. Fluid Mech.*, *14*(1), 213–234.
Smyth, W. D., and J. N. Moum (2000), Length scales of turbulence in stably stratified mixing layers, *Phys. Fluids*, *12*(6), 1327–1342.
Smyth, W. D., J. N. Moum, and D. R. Caldwell (2001), The efficiency of mixing in turbulent patches: Inferences from direct simulations and microstructure observations, *J. Phys. Oceanogr.*, *31*, 1969–1992.
Staquet, C. (1995), Two-dimensional secondary instabilities in a stratified shear layer, *J. Fluid Mech.*, *296*, 73–126, doi:10.1017/S0022112095002072.
Stashchuk, N., and V. Vlasenko (2009), Generation of internal waves by a supercritical stratified plume, *J. Geophys. Res.*, *114*, C01004, doi:10.1029/2008JC004851.
Umlauf, L., and H. Burchard (2005), Second-order turbulence closure models for geophysical boundary layers. A review of recent work, *Cont. Shelf Res.*, *25*, 795–827, doi:10.1016/j.csr.2004.08.004.
Vlasenko, V., N. Stashchuk, and R. McEwan (2013), High-resolution modelling of a large-scale river plume, *Ocean Dyn.*, *63*(11–12), 1307–1320.
Wang, B., O. B. Fringer, S. N. Giddings, and D. A. Fong (2009), High-resolution simulations of a macrotidal estuary using SUNTANS, *Ocean Modell.*, *28*(1–3), 167–192, doi:10.1016/j.ocemod.2008.08.006.
Wang, B., S. N. Giddings, O. B. Fringer, E. S. Gross, D. A. Fong, and S. G. Monismith (2011), Modeling and understanding turbulent mixing in a macrotidal salt wedge estuary, *J. Geophys. Res.*, *116*, C02036, doi:10.1029/2010JC006135.
Zhu, J. (1991), A low-diffusive and oscillation-free convection scheme, *Commun. Appl. Numer. Methods*, *7*(3), 225–232.